Journal of Power Sources 213 (2012) 317–337

Contents lists available at SciVerse ScienceDirect

Journal of Power Sources

journal homepage: www.elsevier.com/locate/jpowsour

Review

Characterization techniques for gas diffusion layers for proton exchange membrane fuel cells – A review

A. Arvay [a], E. Yli-Rantala [c], C.-H. Liu [a], X.-H. Peng [b], P. Koski [c], L. Cindrella [d], P. Kauranen [c], P.M. Wilde [e], A.M. Kannan [a,*]

[a] Fuel Cell Laboratory, Department of Engineering, Arizona State University, Mesa, AZ 85212, USA
[b] Department of Applied Science & Mathematics, Arizona State University, Mesa, AZ 85212, USA
[c] VTT Technical Research Centre of Finland, P.O. Box 1300, FI-33101 Tampere, Finland
[d] Department of Chemistry, National Institute of Technology, Tiruchirapalli 620015, India
[e] SGL Carbon GmbH, Werner-von-Siemens-Strasse 18, 86405 Meitingen, Germany

ARTICLE INFO

Article history:
Received 16 March 2012
Received in revised form
13 April 2012
Accepted 16 April 2012
Available online 16 May 2012

Keywords:
Gas diffusion layer
Conductivity
Porosity
Gas permeability
Water transport
Proton exchange membrane fuel cell

ABSTRACT

The gas diffusion layer (GDL) in a proton exchange membrane fuel cell (PEMFC) is one of the functional components that provide a support structure for gas and water transport. The GDL plays a crucial role when the oxidant is air, especially when the fuel cell operates in the higher current density region. There has been an exponential growth in research and development because the PEMFC has the potential to become the future energy source for automotive applications. In order to serve in this capacity, the GDL requires due innovative analysis and characterization toward performance and durability. It is possible to achieve the optimum fuel cell performance only by understanding the characteristics of GDLs such as structure, pore size, porosity, gas permeability, wettability, thermal and electrical conductivities, surface morphology and water management. This review attempts to bring together the characterization techniques for the essential properties of the GDLs as handy tools for R&D institutions. Topics are categorized based on the *ex-situ* and *in-situ* characterization techniques of GDLs along with related modeling and simulation. Recently reported techniques used for accelerated durability evaluation of the GDLs are also consolidated within the *ex-situ* and *in-situ* methods.

1. Introduction

The proton exchange membrane fuel cells (PEMFCs) are being accepted as promising power sources for automotive, stationary and portable applications due to their higher power densities compared to other fuel cell types. The heart of the PEMFC system is the membrane-electrodes assembly (MEA) consisting of a proton conducting membrane with anode and cathode catalyst layers (CL) and gas diffusion layers (GDL) in contact with each of the CLs. The GDL is a crucial component in the PEMFC and hence an enormous amount of research and development is being carried out by educational institutions as well as commercial organizations.

Membranes with ionic groups that are ionized by water, like perfluorinated sulfonic acid ionomers, need to be hydrated in order to maintain high proton conductivity and ensure adequate fuel cell performance with access to optimum amount of reactants. However, excess water (product water as well as from the humidified reactants) in the electrodes can result in electrode flooding, which prevents chemical reactions from occurring and reduces performance, so a careful balance must be maintained. This can be achieved by designing the GDLs carefully with an appropriate combination of hydrophilic and hydrophobic characteristics. The GDLs are typically wet-proofed with polytetrafluoroethylene (PTFE) to ensure that the pores of the GDL remain relatively dry to avoid flooding with water from the reaction product and the humidified gases [1].

GDLs serve four primary functions: (1) to provide electron conduction to and from the catalyst layer with the through- and in-plane electronic resistivity around 0.08 Ω cm and between 0.055 and 0.009 Ω cm, respectively; (2) to provide reactant transport to and product removal from the catalyst layer with a typical porosity of 0.7–0.8; (3) to provide heat transport from the catalyst layer to the current collector - the through-plane thermal conductivity of cloth and paper GDL varies with PTFE content but has been measured to be between 0.2 and 1.8 W m^{-1} K^{-1}; and (4) to provide mechanical support for the electrolyte structure preventing it from

* Corresponding author. Tel.: +1 480 7271102; fax: +1 480 7271549.
E-mail addresses: amk@asu.edu, amkannan@asu.edu (A.M. Kannan).

0378-7753/$ – see front matter © 2012 Elsevier B.V. All rights reserved.
doi:10.1016/j.jpowsour.2012.04.026

tenting into the channels of the bipolar plate, which results in elevated channel pressure drop, catalyst layer damage, and local water pooling.

The GDL is composed of a sheet of electrically conductive macro-porous substrate, such as a non-woven carbon fiber paper or a woven carbon cloth and a thin (say about 100 μm) micro-porous layer (MPL) of carbon black mixed with PTFE. The MPL improves the water management, reduces contact resistance and also protects the catalyst layer from physical damage caused by the macro-porous carbon substrate [2,3].

The commercial viability of the PEMFCs depends on their ability to perform well with H_2 (or reformate)/air at various operating conditions. GDLs influence the fuel cell performance especially at higher operating current regions by controlling the mass transport of reactants and product water to maintain active sites, especially when reformate and air are used as fuel and oxidant, respectively. Liquid water condensed from the water vapor and produced by oxygen reduction reaction (ORR) at the cathode CL moves into the membrane or the GDL. In the former case, higher liquid water pressure formed by electro-osmotic drag and electrochemical reaction at the interface between the membrane and the CL drives water flow toward the anode. In the latter, liquid water accumulates at the CL/GDL interface and then flows toward the gas flow channels when liquid water pressure exceeds a threshold pressure for water flow through the GDL. The threshold pressure is determined by the GDL pore geometry and hydrophobicity.

The ideal GDL should have properties such as good gas diffusion with optimum bending stiffness, porosity, tortuosity, thickness, surface contact angle, air permeability, water vapor diffusion, electronic conductivity, crack free surface morphology, high mechanical integrity and enhanced oxidative stability along with durability at various operating conditions including freeze/thaw [4,5]. A review by Park et al. [6] addressed recent developments of single- and dual-layer GDLs with various types of carbon materials and approaches with a variety of carbon- and metal-based macro-porous substrates using different fluorinated hydrophobic polymers. Our recent review in 2009 in the *Journal of Power Sources* highlighted the methods of preparation, structure, and performance characterization of GDLs [7]. The present paper focuses specifically on the techniques used for evaluating GDLs both by *ex-situ* and *in-situ* methods including accelerated durability.

2. Characterization techniques

The GDL characteristics influencing fuel cell performance depend on the type of materials and the process of fabrication of the substrate as well as the MPL. The characterization techniques in the following sections are categorized based on *ex-situ* (GDLs alone) and *in-situ* (within the fuel cells) methods. The characterization techniques include the use of novel tools and processes as well as standardized methods and commercial equipment developed and/or modified for GDL materials. The methods discussed are appropriate for quality control in large scale production and/or small batches of prototype material in the R&D lab.

2.1. Ex-situ methods

Various GDL properties, such as electrical and thermal conductivity, porosity, and morphology, can be examined by *ex-situ* methods. The *ex-situ* characterization can be conducted for pristine GDLs or as *post-mortem* analysis. The results of *post-mortem* analysis can give secondary information about the possible failure modes in GDLs, if compared to the properties of the pristine sample. Accelerated aging of the GDLs can also be performed artificially, or *ex-situ*. It is beneficial to design the artificial aging treatment so that the effects of accelerated aging are in relation to what would occur in the GDLs in a real PEMFC environment over a certain time of operation.

2.1.1. Electrical conductivity

Good electrical conductivity of the GDLs correlates directly with fuel cell performance [8]. When measuring the electrical conductivity of GDLs, it should be noted that the clamping pressure affects the conductivity by reducing the contact resistances. Therefore, the measurements are usually conducted under a pressure of 1 MPa, as it is the commonly used clamping pressure in PEMFCs [9]. A four-point probe method [10] is generally used to measure low resistances because the contact resistance between the sample and the probe can be neglected. This is in contrast to the two-point probe method, where the contact resistance is included in the measured resistance [11].

2.1.1.1. Through-plane electrical conductivity. Through-plane resistance measurement in its simplest form consists of placing a GDL sample between two highly conducting plates or rods, applying a defined compression and a DC current, then measuring the plate-to-plate voltage drop. The through-plane resistance is expressed in units of Ω cm^2 and it includes the contributions from the bulk material and the two contact resistances between the GDL sample and plates. It is possible to distinguish the bulk resistance from the contact resistance provided that the same GDL material is available in a variety of thicknesses. The bulk resistance contribution ($R_{z,bulk}$) can be expressed as

$$R_{z,bulk} = \rho_z d \tag{1}$$

where ρ_z is the through-plane resistivity and d is the GDL thickness. The measured resistance in ohms, $R_{z,meas}$ can be expressed as

$$R_{z,meas} = \frac{2R_{contact} + 2R_{z,bulk}}{A} \tag{2}$$

where $R_{contact}$ is the contact resistance between the sample and plate. Each of the values, with the exception of the sample area A, in the above two equations depends on the applied compression [8]. In the through-plane direction the contact resistance is the major factor affecting the conductivity [9].

The commonly used standardized method for the through-plane conductivity measurement procedures is Standard Test Method for Electrical Resistivity of Manufactured Carbon and Graphite Articles at Room Temperature (ASTM C611-98 (2010) e1) [12]. This method is in use by fuel cell component manufacturers such as E-TEK [13], CeTech [14], and FuelCellsEtc [15], and has also been used by Williams *et al.* [16] in their GDL characterization studies. However, according to Ismail *et al.* [9] the method was originally designed to measure the electrical resistivity of carbon blocks, not thin carbon sheets, and therefore its applicability to GDLs is questionable.

A through-plane conductivity measurement setup designed by Ismail *et al.* [9] is illustrated in Fig. 1a. In this setup the GDL sample is placed between two stainless steel discs representing the bipolar plates of a fuel cell. The GDL and the discs are sandwiched between two copper electrodes by a bolt that allows compression with progressively increasing increments. The total resistance of the assembly is then measured at each compressive pressure by an ohmmeter. The effect of pressure on the through-plane conductivity of GDLs with or without an MPL and with varying PTFE loading was investigated. It was found that the contact resistance increases when PTFE content is increased and the presence of MPL reduces the contact resistance.

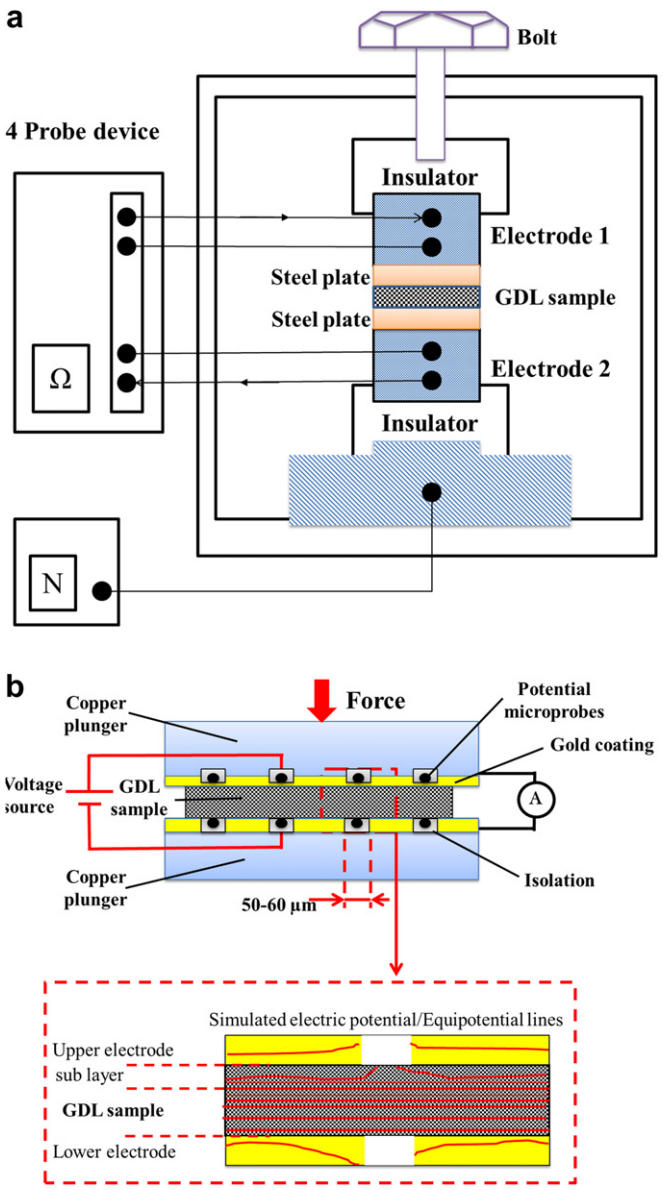

Fig. 1. (a) Schematics for through-plane electrical conductivity measurements as adopted from [9] and (b) from [17].

The through-plane conductivity upon compression of Toray and some unidentified roll-good carbon papers was studied by Kleemann *et al.* [17] for modeling purposes. The device they used was based on two gold plated copper plates, where four potential-sensing microprobes were embedded, as shown in Fig. 1b. The figure also shows an electrical FEM-simulation of the setup with potential distribution and equipotential lines in the sample. This study observed compression dependent decrease in through-plane resistance for all GDL types ranging from greater than 50 mΩ cm^2 at low compression to less than 5 mΩ cm^2 at compressions >1 MPa.

2.1.1.2. In-plane electrical conductivity. Through-plane electrical conductivity is the most often measured electrical property of GDLs despite the fact that in-plane conductivity is also crucial for fuel cell operation. The GDL is not entirely in contact with the bipolar plate due to the flow channels, and therefore the in-plane electrical conductivity can compensate for the poor through-plane conductivity underneath the flow channels. Ismail *et al.* [9] determined the in-plane conductivity of GDLs with a simple device shown in Fig. 2. In-plane measurements were conducted on samples containing 0–30 wt. % PTFE. It was observed that the in-plane conductivity of carbon papers does not depend on PTFE content. In contrast, it was found that the conductivity heavily depends on the measurement direction: the conductivities in two perpendicular in-plane directions differ by a factor of about two, from over 50 S cm^{-1} to less than 30 S cm^{-1}, because of the preferential orientation of the carbon fibers [9].

Based on the measurements conducted by Kleemann *et al.* [17], it was concluded that the in-plane conductivity increases linearly with increasing compression. Their test device consisted of a printed circuit board with four-point-probe configuration fixed between two pressure plates. A technique referred to as Van der Pauw method (vdP) [18] was used in in-plane resistivity measurements of Toray carbon papers by Li *et al.* [19]. In general, this method is suitable for the resistivity measurements of thin samples of arbitrary shape but requires constant thickness and a uniform resistivity [20]. In the described measurement, square carbon paper samples were connected to a four-probe station from each corner. It was found that the in-plane conductivity is lower for PTFE treated carbon papers when compared to the carbon paper without wet proofing, which is contrary to the findings of Ismail *et al.* [9].

2.1.2. Thermal conductivity

Operating PEMFCs produce an amount of heat comparable to their electrical power output. The membrane is very sensitive to excessive heat and can be damaged if temperatures exceed 100 °C, so effective thermal management of the cell is needed. Removing the waste heat produced in an operating fuel cell is one of the important functions of the GDL. Good thermal conductivity of a GDL facilitates removing the waste heat and prevents large temperature gradients from forming within the cell [21].

The thermal conductivity of the GDL depends on several factors including compression, PTFE content, temperature, and the presence of liquid in the pores. Compression applied to the GDL can create better physical contact between individual carbon fibers which increases overall thermal conductivity [22]. The effect of temperature on the thermal conductivity is important since PEMFCs are designed to operate at various temperatures depending on the application [23]. Furthermore, water within the GDL, both in form of liquid and gas, affects the thermal conductivity [24].

2.1.2.1. Through-plane thermal conductivity. Thermal transport properties, similarly to electrical properties, differ significantly in the through-plane and in-plane directions because of the anisotropic micro-structure of the carbon paper [25]. Various methods for determining the through-plane thermal conductivity are cited in literature. Zamel *et al.* [22] examined the through-plane thermal conductivity of carbon paper by a thermal capacitance (slug)

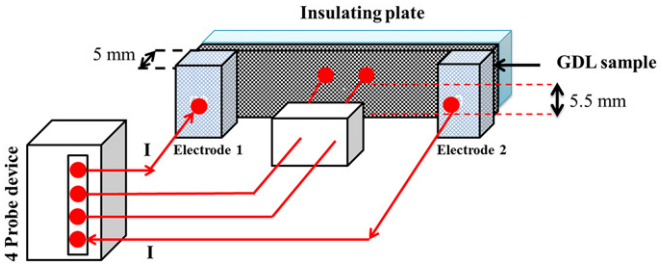

Fig. 2. Schematic for in-plane electrical conductivity measurements as adopted from [9].

method. The method follows the ASTM standard E2584-07 (Standard Practice for Thermal Conductivity of Materials Using a Thermal Capacitance (Slug) Calorimeter). This has since been superseded by ASTM E2584-10 [26,27]. The method in question is based on the assumption of one-dimensional heat flow through the carbon paper sample. A schematic of the through-plane measurement setup is shown in Fig. 3a. In the studies conducted by Zamel *et al.* [22], the combined effect of temperature, compression and PTFE loading on the through-plane thermal conductivity of a Toray carbon paper was measured. As presumed, the thermal conductivity was seen to increase upon increasing the compression both in the case of untreated and PTFE treated carbon paper. In addition, they also observed that an increase in temperature resulted in improved through-plane thermal conductivity. This behavior is in contrast with observations from in-plane thermal conductivity studies [23] indicating that the thermal expansion of the carbon fibers is a direction-dependent property [22].

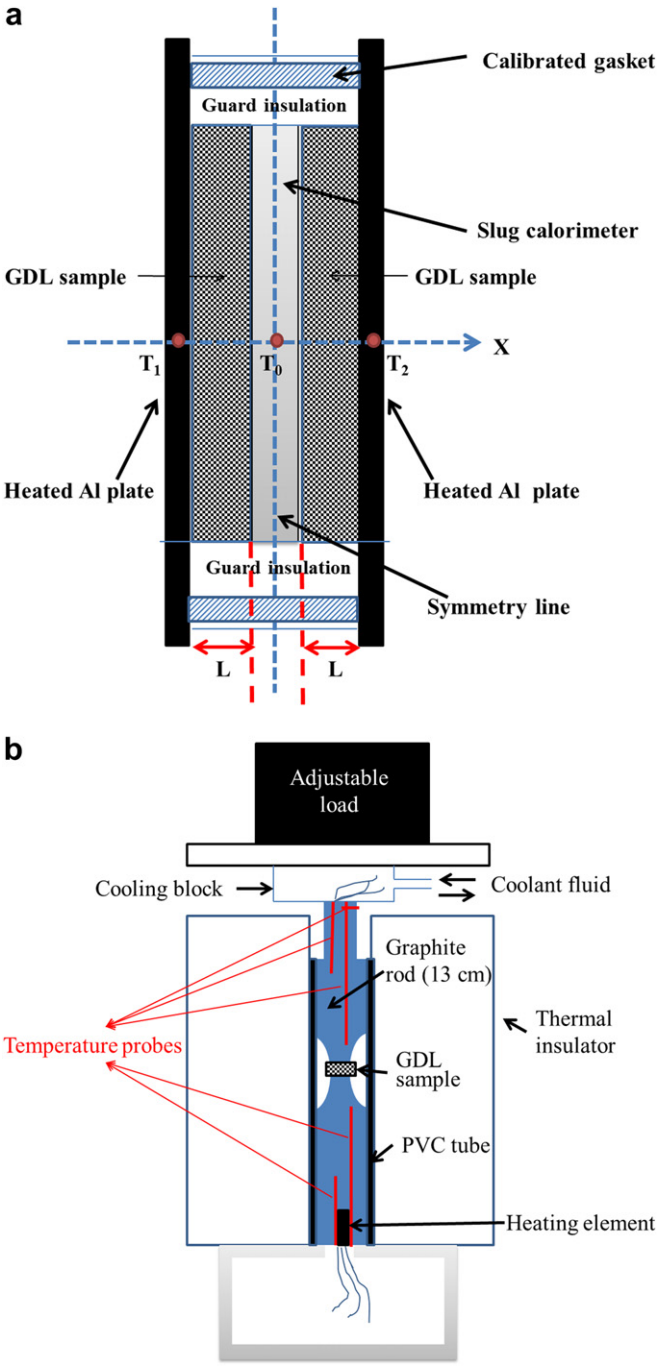

Fig. 3. (a) Schematics for through-plane thermal conductivity measurements as adopted from [22] and (b) [30].

Another standardized method used in GDL thermal conductivity determination is ASTM standard D5470-06 (2011) (Standard Test Method for Thermal Transmission Properties of Thermally Conductive Electrical Insulation Materials) [28]. The method was employed in a modified version by Karimi *et al.* [29] to study the thermal conductivity of GDLs over a compression range from 0.07 to 1.38 MPa. According to their findings the PTFE loading seemed to enhance the effective thermal conductivity at low compression loads, whereas at higher compression loads the effect was the contrary.

Nitta *et al.* [30] measured the thermal properties of the GDL by employing a measurement setup where the GDL sample was placed between two graphite rods and a heat flux from a heating element embedded in the lower rod was transferred to the upper rod through the GDLs. The measurement system is illustrated in Fig. 3b. In these measurements it was observed that the thermal conductivity does not seem to depend on compression, whereas the thermal contact resistance decreases with increasing compression. Furthermore, the measured thermal conductivity value of the GDL is about four times larger than those reported in literature. The latter was explained by taking the thermal contact resistances into account [30].

Another method allowing the characterization of the GDL thermal conductivity as a function of the applied mechanical compression has been developed by Hamour *et al.* [31] using the transient hot-wire technique (THW). THW technique is best known for the characterization of the thermal conductivity of fluids, but has now been successfully applied to solid matter as well. The advantage of the THW technique is that it allows the thermal conductivity determination without the problem related to the contact resistance. The method is based on measuring the dynamic temperature response of a long wire embedded in the sample material. The wire is heated by a constant electrical current, which results in a nearly constant line source of a heat flux in the sample. When increasing the compression pressure up to 8 MPa, it was observed that the thermal conductivity of the carbon cloth increases with increasing compression. Furthermore, the behavior of the thermal conductivity as a function of applied pressure was discovered to agree well with the mathematical equation established as a theoretical solution to the problem [31].

2.1.2.2. In-plane thermal conductivity. Until recently, only a few studies concerning in-plane thermal conductivity measurements of GDLs have been published. It is challenging to accurately measure the heat flux through a sample with a thickness on the order of hundreds of micrometers [23]. Sadeghi *et al.* [25] investigated the in-plane thermal conductivity of a Toray carbon paper with varying PTFE content. In their experimental setup, the GDL samples were supported from their outer edges by two sample holders. The first sample holder was connected to a flux meter that was, in turn, connected to an electrical heater. The other sample holder was connected to another flux meter that was integrated with a cold plate. The measurement setup is schematically illustrated in Fig. 4a. According to this study, the in-plane thermal conductivity remains almost unchanged regardless of the PTFE content, which was varied from 5 to 30%. As reported in literature, the in-plane and through-plane thermal conductivity values are 3.5–15 and 0.2–2 $W\,m^{-1}\,K^{-1}$ for various GDL materials [23].

Zamel *et al.* [23] studied the effect of PTFE loading on the in-plane thermal conductivity of a Toray carbon paper in

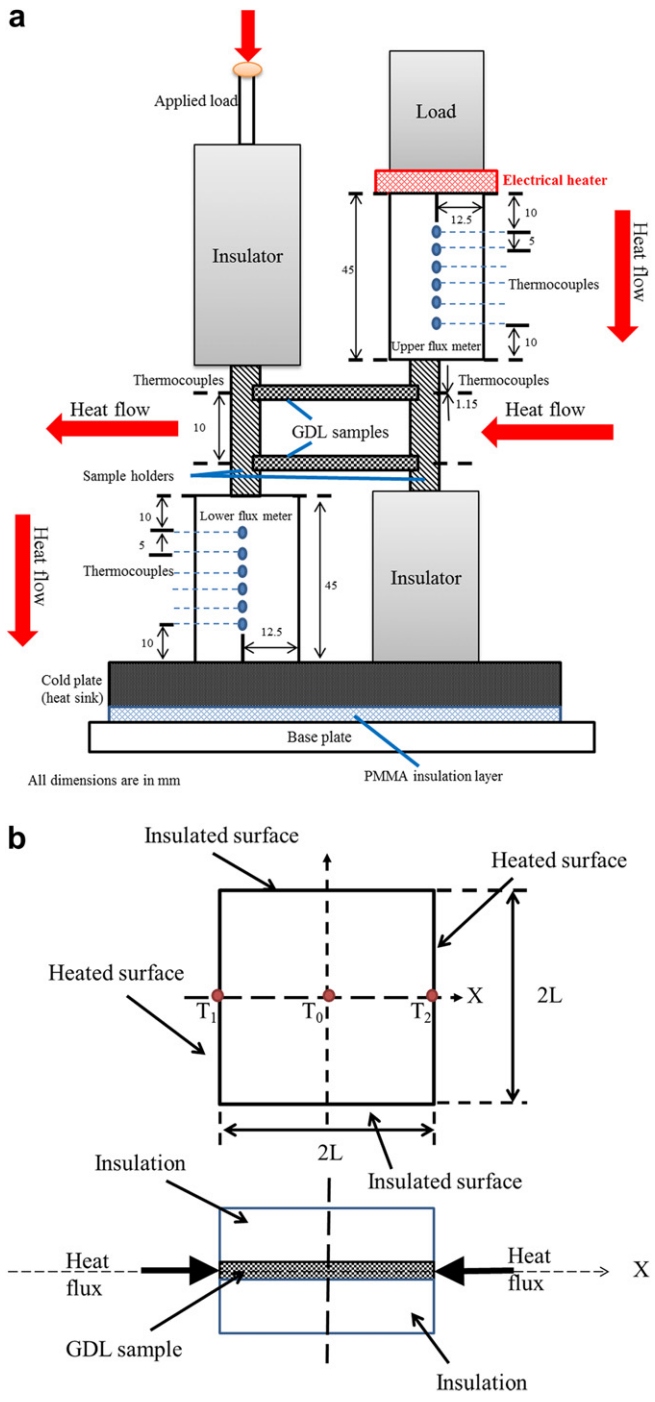

Fig. 4. (a) Schematics for in-plane thermal conductivity measurements as adopted from [25] and (b) [23]. T_0, T_1 and T_2: GDL sample and hot platens temperatures, respectively; X: centroid line; and L: distance between the center and the edge of the GDL sample.

a temperature range from −20 to +120 °C using a monotonic heating regime in quasi-steady conditions. In a monotonic heating regime the temperature increases with the same and constant rate in all points of the sample. The employed test setup is presented schematically in Fig. 4b. A multi-layer sample composed of several layers was used. The sample, with a thermocouple mounted in the middle of the sample between the layers, was sandwiched from two opposing sides between two heated aluminum plates. This study revealed that the in-plane thermal conductivity decreases from 25 to 12 W m^{-1} K^{-1} with increasing temperature from −20 to 120 °C for GDL without any PTFE. It was also shown that only 5 wt. % PTFE content is enough to decrease the in-plane thermal conductivity to 12 W m^{-1} K^{-1} at all temperatures. However, further addition of PTFE does not seem to lower the conductivity in the same proportion [23].

2.1.3. Mechanical properties

Optimal mechanical properties of GDLs are also crucial for the good performance of a PEMFC. A sufficiently high mechanical strength of the GDL prevents it from significantly intruding into the gas channels of the bipolar plates when compression is applied to the cell. Since the intrusion of the GDL is likely to result in reduced mass transport capacity and poor electrical and thermal contact between the GDL and bipolar plate, high mechanical strength of the GDL is vital for achieving the maximum performance of PEMFC [32,33]. In addition, the GDL should have some elasticity in order to compensate for the volume changes of the electrolyte membrane due to changes in the level of hydration and during freeze/thaw [34]. Mechanical properties are highly anisotropic due to preferential orientation of carbon fibers in the GDL substrate. This means that certain properties may differ significantly in the machine direction (MD) compared to the cross-machine direction (CMD) [32].

2.1.3.1. Tensile strength. There are several standardized methods for the determination of tensile properties, namely (ultimate) tensile strength, tensile strength at break, yield strength and elongation. Although tensile stress is widely absent in fuel cell operation, tensile strength is important material parameter considering continuous production of the GDL material and further treatment for example subsequent coating or lamination processes. Among carbon paper manufacturers the most commonly referred method is ASTM standard D828-97 (2002): Standard Test Method for Tensile Properties of Paper and Paperboard Using Constant-Rate-of-Elongation Apparatus [13–15]. This standard is however withdrawn in 2009 without replacement [35]. Another standard in use by QuinTech [36] and Freudenberg [37] is DIN EN 29073-3:1992, Textiles; Test methods for non-wovens; Part 3: Determination of tensile strength and elongation [38]. Hung *et al.* [39] employed the ASTM standard D638-10 titled as Standard Test Method for Tensile Properties of Plastics [40] on GDL characterization. Ha *et al.* [41] investigated the effect of accelerated carbon corrosion on tensile properties of electrochemically oxidized GDLs by a specifically designed tester. It was observed that the tensile strength at break in the MD is higher than in the CMD, and the accelerated carbon corrosion lowered both tensile strength and elongation at break, especially in the MD.

2.1.3.2. Compressibility. Since the GDL is a porous structure, the thickness can be measured as part of the compressibility tests with specific loads. The compressibility or compressive stress–strain behavior of a GDL can be determined by placing it between two flat plates and measuring the deflection as a function of the compressive force. The procedure can be repeated several times for the same sample in order to observe the elasticity and weakening behavior of the material. Reduction in initial thickness, which refers to residual strain, may be observed when the load is removed [8]. Compressive behavior of SGL Sigracet 10 BA was measured by Nitta [42] with an experimental setup as illustrated in Fig. 5. The study was conducted by applying various compression forces by changing the loading weight, the maximum compression pressure being 5.5 MPa. Nitta observed three distinctive regions in the stress–strain curve: 0–0.2, 0.2–3.5 and 3.5–5.5 MPa. The first region at low compression pressure, where the strain is increasing

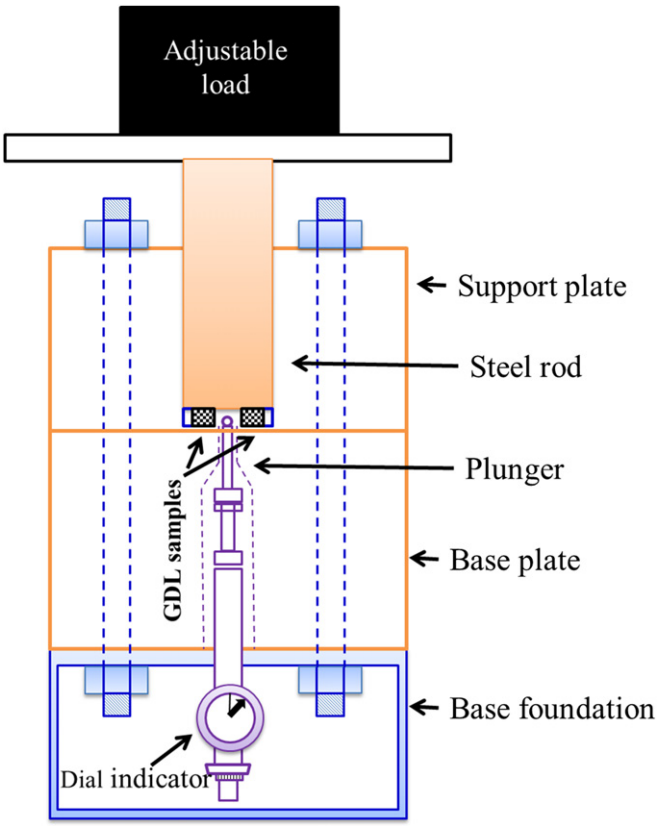

Fig. 5. Schematic for compressibility measurement as adopted from [42].

fastest, was associated with smoothening of the rough surface of the GDL. The second and third regions were concluded to be due to crushing of the hydrophobic and hydrophilic pores, respectively.

Han *et al.* [43] examined the effect of compression on the thickness variation of several commercial GDL samples. Using a bipolar plate underneath the sample enabled studying also the intrusion effect. The results suggested that GDLs are typically more resistant to compression in the CMD compared to the MD, especially in the case of fiber-felt type GDLs. The anisotropy effect seems to be less significant for carbon fiber-paper type GDLs. It was also concluded that the degree of intrusion of GDL into the gas channels may be lower in cases where flow field channels are oriented perpendicular to the MD compared to parallel direction. Other studies concerning compressive behavior of GDLs include examination of the local compressibility [17,44] and the hysteresis effect resulting from cyclic compressive load [45]. The GDLs could also be evaluated for short-time compressibility and recovery using an ASTM standard for gasket materials [46].

2.1.3.3. Flexural or bending properties. High flexural strength is especially important in cost-efficient roll-to-roll manufacturing processes of the GDLs and MEAs. There are several methods for determining the flexural behavior of carbon papers. The methods are based on measuring the force applied in the center of the sample as a function of displacement, i.e. bending. The flexural modulus is defined by the force–displacement curve and the force at break determines the flexural strength [8]. Bending stiffness is highly direction dependent property, usually being higher in the MD compared to CMD [33].

Kleemann *et al.* [17] determined the bending behavior of GDLs following ISO standard 5628:1990 Paper and board – Determination of bending stiffness by static methods – General principles. The standard is revised in 2012 [47]. This standard includes 2-point, 3-point and 4-point methods, of which the 3-point method is the most commonly applied technique. The 3-point bending principle is illustrated in Fig. 6 [48]. Results from 3-point bending tests performed by Kleeman *et al.* showed that batch-fabricated material (TGP-H-060) had a bending modulus of over 9 GPa while roll-good materials were all less than 2 GPa. They also found bending modulus was a direction dependent property.

Other standardized methods for the evaluation of flexural behavior used in GDL characterization [8,14] include ASTM D790-10 (Standard Test Methods for Flexural Properties of Unreinforced and Reinforced Plastics and Electrical Insulating Materials) [49] and in studies [50,51] ASTM D1184-69 Standard Test Method for Flexural Strength of Adhesive Bonded Laminated Assemblies, of which active form is D1184-98-2004 [52]. The readers can refer to the ASTM standards for more details.

2.1.4. Porosity and pore size distribution

One of the advantages of carbon paper and cloth as GDL substrates is that their porosity can be controlled, which allows for uniform distribution of the reactant gases. The PEMFC performance is strongly influenced by interdependent properties such as water and gas transport of GDL comprising macro- and micro-porous layers. Balanced properties of hydrophobicity (water expelling) and hydrophilicity (water retaining) are also needed to ensure optimum fuel cell performance in various humidity conditions. Water management is essential for effective and steady operation of PEMFCs, which requires the membranes to be hydrated and the MEAs not to be flooded. Kong *et al.* evaluated multiple GDL samples using mercury porosimetry and determined that a bimodal pore-size distribution improved overall fuel cell performance. The bimodal distribution contained macropores ranging from 5 to 20 microns and micropores ranging from 0.03 to 0.06 microns [53]. Numerical models developed by Chu *et al.* predicted that continuous porosity gradients would improve fuel cell performance primarily at high current densities [54]. There are several methods to determine the porosity and pore size distribution. Intrusion methods using kerosene, mercury or water and capillary flow porometry are the most popular methods.

The following techniques are simple to perform and give a quantitative measure of porosity and pore size distribution, which are useful for comparing different GDL samples. They all make a general assumption that the capillary structure can be represented by a bundle of tubes with a particular range of radii. This simplifying assumption does not accurately capture the complex pore structure of a GDL. Inferences about the internal structure drawn from such measurements should be made with careful

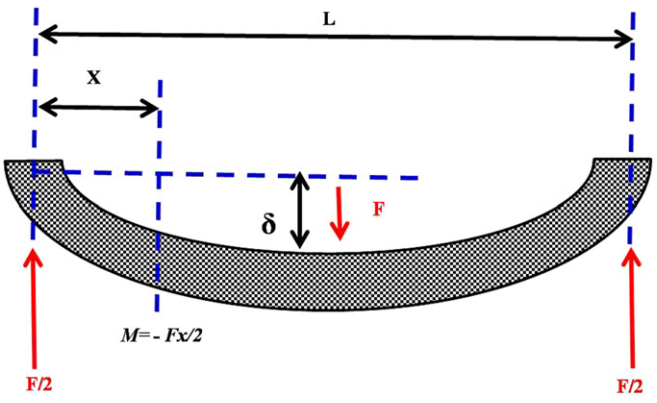

Fig. 6. Schematic for three-point bending as adopted from [48].

consideration. New methods, such as hydraulic admittance [55] are under development which may lead to more accurate information about the complex pore structures found in GDLs.

2.1.4.1. Kerosene based method. Mathur *et al.* [56] determined the porosity of carbon paper samples by kerosene density method [57]. Density measurements were made by first measuring the sample weight then submerging the sample in kerosene and measuring the displacement. A non-polar liquid like kerosene is not affected by the hydrophobicity of the GDL material and will penetrate all of the pores. The porosity of the carbon paper substrate shows a decreasing trend with increasing sintering temperature [56]. The porosity is as high as 72% for the samples heated to 1000 °C and reduces to about 66% as the temperature increases to 2500 °C. Porosity measurements based on liquid displacement are relatively easy to perform but the lack of pore size distribution data makes them less useful for GDL characterization.

2.1.4.2. Mercury intrusion porosimetry. Intrusion porosimetry determines the porosity and the pore size distribution by using high pressure to force liquid into the pores of a sample. Information about the pore size distribution can be derived from the pressure required to overcome the surface tension. Mercury (Hg) is a commonly used liquid for porosimetry because it has high surface tension ($\sigma = 486.5$ mN m^{-1}). This property makes the fluid non-wetting so that Hg intrusion is not affected by hydrophobicity of the material. Hence, Hg intrusion porosimetry can be used to determine the distribution of both hydrophobic and hydrophilic pores and also provides a wide range of measurable pore radii from 10 nm to 150 μm.

When an external pressure is applied, all pores with radii $r > r_{min}$ become filled with Hg. The value of r_{min} corresponds to the condition that the Hg capillary pressure P_c in the pore is equal to the applied pressure. The capillary pressure is determined by the thermodynamic Laplace equation:

$$P_c = 2\sigma\frac{\cos\theta}{r_{min}} \tag{3}$$

where σ is the surface energy or surface tension and θ is the wetting angle of liquid Hg with the given material. The pore radii and pore volume are estimated from the applied pressure and the volume of Hg.

Pore size distribution of a typical GDL shows micro, meso- and macropores of 0.06, 0.2 and 55 μm diameter, respectively. Quantachrome PoreMaster-33 and Micromeritics AutoPore IV-9500 are the typical instruments to analyze any porous media with pore sizes ranging between 3 nm and 200 micron sizes. Hg intrusion porosimetry is one of the valuable techniques in optimizing the pore size distribution of GDLs for PEMFC operation at different RH conditions [58]. However, the GDLs deform or are even destroyed due to extremely high pressure (hundreds of MPa) required to fill smaller pores with Hg during the measurement. Hg also requires special handling due to its health and environmental hazards.

2.1.4.3. Water intrusion porosimetry. Water intrusion porosimetry uses the same principles as Hg porosimetry but uses a different working fluid. Water is non-toxic and has a lower surface tension than Hg which reduces the pressures required to fill the pores. Lower pressures reduce the complexity of the equipment and decrease the likelihood of damaging the test sample. However, water intrusion porosimetry is only able to determine the distribution of hydrophobic pores. The concept of a water porosimeter is that the sample is held between hydrophilic and hydrophobic porous membranes. Water is added and removed through the hydrophilic side while gas pressure is applied through the hydrophobic side. The water is added at a range of pressures that ensure that the hydrophilic membrane is always full of water and the hydrophobic membrane always empty. The capillary pressure curve for the sample can be generated from this procedure.

Harkness *et al.* [59] used a novel water intrusion porosimeter to predict the water handling behavior of GDL when placed under a compressive load. The schematic of the porosimeter used for this work is depicted in Fig. 7. The sample is compressed in a fixture consisting of two aluminum alloy end plates, one of which has a pneumatic piston mounted in it. This piston can exert compressive loads on the GDL sample up to ~0.7 MPa to simulate similar degree of compression that would be used in a typical fuel cell assembly.

2.1.4.4. Capillary flow porometry. Capillary flow porometry uses similar principles as intrusion porosimetry. Instead of using a non-wetting fluid and forcing it into the pores as in intrusion porosimetry, capillary flow porometry first fills the pores with a wetting fluid and uses pressurized gas to drive the liquid out. Water can be used in this method to determine the distribution of hydrophilic pores. A fully wetting fluid such as octane can be used to determine the distribution of both hydrophilic and hydrophobic pores.

First, gas pressure and flow rates through the dry material are accurately recorded. Bulk material porosity is measured by weighing the sample before and after immersing it in a wetting liquid of known density [16]. Once the pores have been filled, a non-reacting gas is introduced to displace the liquid from the pores. The gas pressure required for removing liquid from the pores and causing gas to flow is given by modifying Eq. (3) to:

$$D = \frac{4\gamma\cos\theta}{P} \tag{4}$$

where D is the pore diameter, γ is the surface tension of liquid, θ is the contact angle of liquid, and P is the pressure difference between liquid and gas. A pore size distribution function, f is defined as

$$f = -\frac{100\left(\Delta\frac{F_w}{F_d}\right)}{\Delta D} \tag{5}$$

where F_w and F_d are wet and dry gas flow rates, respectively. The pore size distribution function is calculated from the variation of the flow rate with the differential pressure for the through-plane flow [60].

Capillary flow porometry can be performed with any wetting liquid as the working fluid. Using water as the working fluid permits one to determine the distribution of hydrophilic pores only. The distribution of the overall porosity can be obtained by

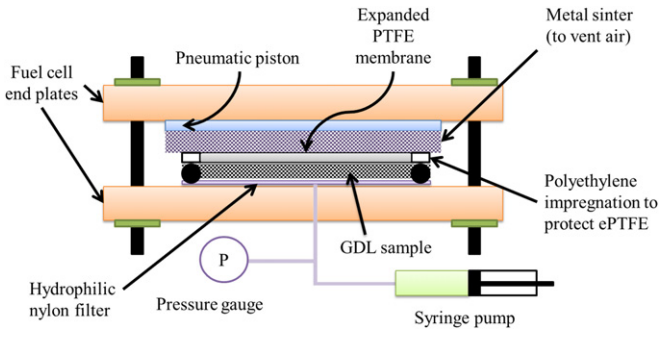

Fig. 7. Schematic of the water porosimeter for pore size distribution as adopted from [59].

using a strongly wetting fluid such as octane, which fully wets both graphite and PTFE surfaces. Capillary flow porometry is better than the intrusion porosimetry based methods as it is relatively faster and also non-destructive for hydrophobic MPLs. The ratio of hydrophobic and hydrophilic pores could be characterized by using a combination of the results from capillary flow porometry, Hg intrusion porosimetry and water intrusion porosimetry [61].

2.1.4.5. Bubble-point method. The bubble-point method is a particular approach to capillary flow porometry and has become a widely adopted and well understood technique [8] with the procedure described in ASTM standards [62]. Mean flow pore size data for the GDL can be estimated by measuring the threshold pressure by bubble-point method using air [8]. In general, for a given fluid and pores with a constant wetting, the pressure required to force an air bubble through the pore is inversely proportional to the pore diameter. In the test setup, the MPL surface of the GDL is placed in contact with a wetting liquid and the GDL material side is exposed to air with regulated pressure. The air pressure is gradually increased until the formation of bubbles at the MPL surface is observed. The main difference between capillary flow porometry and the bubble-point method is the observation of the initial bubble which determines the size (and location) of the largest pore, the open bubble-point pressure determines the mean pore size of the GDL.

Fig. 8 compares the bubble-point pressure of Vulcan XC-72R and Pureblack + nano-fibrous carbon and Vulcan XC-72R GDLs [63]. The GDL with Pureblack + nano-fibrous carbon show lower bubble-point pressure (0.16 psi as against 0.46 psi) due to the presence of larger pores compared to that with Vulcan, as the pore radius is inversely proportional to bubble-point pressure (see Eq. (3)). The mean flow pore diameter can be calculated for pure black/nano-fibrous carbon based GDL from the pressure by Eq. (4) and then averaging over all the pressure values. The resulting average diameter is only about 24 μm. Therefore, it is expected that there will not be any additional restriction to gas flow for this micro-porous coating. Bubble-point pressure helps optimizing GDLs for various operating conditions. Bubble point pressure method can also be used for characterizing porous carbon bipolar plates [64]. Capillary flow porometry was used to determine pore sizes of various paper type GDLs under varying degrees of PTFE content and compression [65]. It was found that pore diameters increased upon compression which was explained by a partially collapsing pore wall structure leading to larger pore diameters.

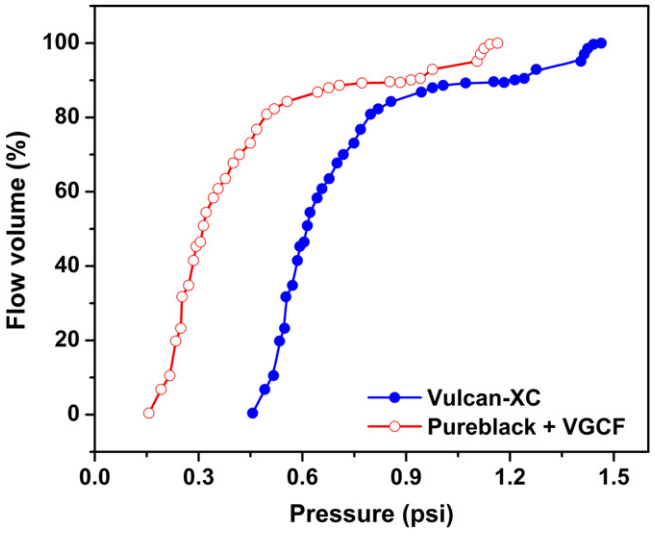

Fig. 8. Bubble-point pressure for Vulcan XC-72R and Pureblack + nano-fibrous carbon based GDLs [63].

2.1.5. Gas permeability

Ensuring effective mass transport is one of the main functions of the GDL, which is why a good gas permeability of the material is crucial [66]. In fuel cells, electronic resistivity is reduced by increasing the clamping pressure whereas permeability, and therefore the mass transport, is reduced by it. There is a clear trade-off between low electrical contact resistivity and good permeability [65]. Permeability, like many other GDL properties, is anisotropic and should optimally be measured in both through-plane and in-plane directions [66].

Through-plane air permeability of carbon papers is most often determined by the Gurley method [67]. The Gurley second or Gurley unit is a unit describing the number of seconds required for 100 cm^3 of air to pass through 1.0 square inch of a given material at a pressure differential of 1.30 MPa [67]. Similar procedures to measure single phase permeability can be made by measuring flow rates and pressure drop through a GDL sample and applying Darcy's law:

$$k = \frac{v_g \mu_g \Delta x}{\Delta P_g} \tag{6}$$

where k is the permeability, μ_g is the gas viscosity, v_g is the gas velocity, ΔP_g is the pressure drop across the gas travel path Δx. If the GDL sample is small then the gas velocity can be assumed to be constant because the pressure drop is low [68]. In order to better replicate the pore structure of the GDL inside a fuel cell, the material can be compressed before the measurements [69,70].

The gas permeability can be measured in two perpendicular in-plane directions as well as the more commonly measured through-plane direction in order to investigate the anisotropic permeability properties of a GDL sample. In the study conducted by Gostick *et al.* [71] the sample was compressed between two plates with variable spacing. This setup enabled measurements of permeability as a function of the GDL thickness. The inlet pressure was controlled by a pressure gauge, and the flow rate was measured on the outlet side using a digital flow meter. GDL permeability showed an exponential relation with compressed volume fraction, where compressing the sample to half its original volume would lead to a 6× reduction in permeability [71].

Hussaini and Wang [72] used steady state methods to measure the relative permeability in the through and in-plane directions in regimes of actual fuel cell operation. Relative permeability measurements are necessary when there is multiphase flow in a porous medium. In a steady state method, two fluids are passed at a known ratio until saturation and pressure reach a steady state. Steady state methods are more suitable for measuring relative permeability at the conditions found in a typical PEMFC. Their study found that carbon paper materials have higher in-plane permeability than through-plane permeability by about 18%. However, carbon cloths have higher through-plane permeability measurements that are 75% higher than in-plane values.

2.1.6. Surface morphology

Scanning electron microscope (SEM), atomic force microscope (AFM) and laser profilometer are the key characterization tools for the GDL morphology as it can clearly provide information of the surface roughness, mud-cracks, valleys etc [73]. Fig. 9a shows the SEM image of the non-woven carbon paper substrate, revealing the network of carbon fibers with 5–10 μm diameter and the open

pores. Fig. 9b and c show the surface morphology of MPL at lower magnifications (35× and 1000×), fabricated using Pureblack carbon by a semi-automatic coating process. Evidently, the MPL is not uniform and suffers seriously from so-called mud-cracking. As seen from Fig. 9a and e at low and high magnifications (1000× and 20,000×), the surface of the MPL could be improved by water based slurry of Pureblack carbon (75 wt.%) with 25 wt.% nano-fibrous carbon showing homogeneous carbon distribution and crack free surface morphology for uniform gas distribution. These SEM images also explain the mechanical characteristics of the MPL's reinforcement by the presence of carbon nano-fibers. The nano-fibers are not ordered and they are entangled both in and through the plane to provide structural integrity of the MPL to the carbon paper substrate. Fig. 9f shows SEM image of *in-situ* grown multi-wall carbon nanotubes (MWCNTs) on non-woven carbon paper substrate. Each fiber of the macro-porous carbon paper is homogenously covered by the micro-porous layer of MWCNTs [74].

Atomic force microscopy can be used in addition to SEM to investigate the surface morphology. AFM can reveal other surface characteristics such as distribution of adhesion forces and conductive areas [73]. A profilometer (MicroXAM Laser Interferometric 3D Surface Profiler) can be employed to measure the surface profile of carbon paper in 2D and 3D. The through-plane heights and depths are used to calculate the average material surface roughness of the MPL [74]. The topography of the MPL as well as the carbon paper can be examined using the 3D digital microscope (Keyence, NJ, USA). Fig. 10a and b compares the topography of the MPL with a non-woven carbon paper substrate using Keyence VHX-600E 3D digital microscope. The 3D image of the MPL surface appears to be uniform compared to the carbon paper substrate where less crests and troughs can be observed [75].

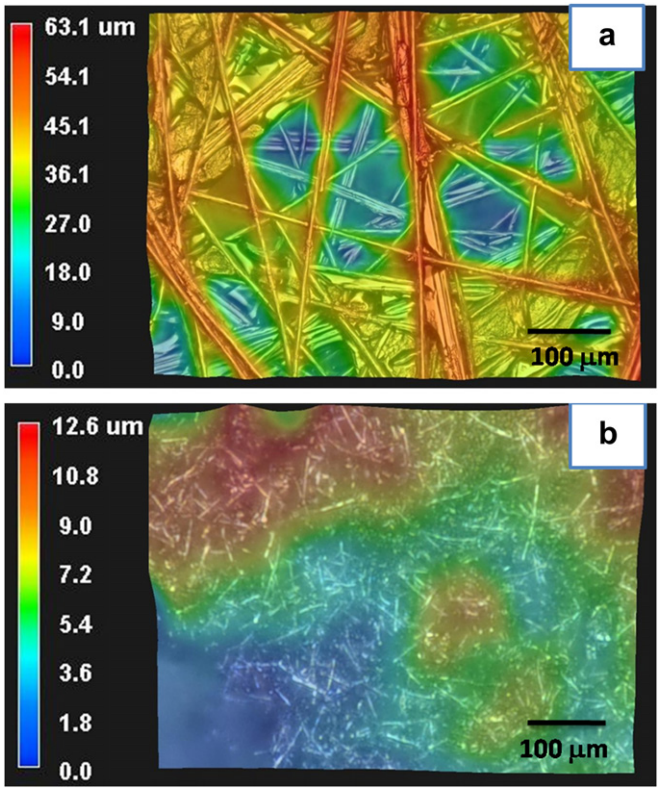

Fig. 10. 3D topographic images of (a) carbon paper substrate, (b) MPL.

2.1.7. Cross-section morphology

The cross-section of the GDL can be analyzed by SEM or focused ion beam (FIB) to understand the morphology of the substrate and MPL [74]. The GDL sample could be prepared for examination of cross-section using SEM by freeze fraction in liquid N_2 or molding it in epoxy resin with subsequent thermal curing and ultra-microtome. However, if FIB is used, the GDL can be sliced *in-situ* by gallium (Ga) ion gun without disturbing the porous structure. The GDLs are examined as part of the MEA without separating them for any post-mortem analysis, as separating the GDLs from the MEA can damage them. Examples of cross-sectional FIB images are presented in Fig. 11. Fig. 11a shows the MPL detailing the nano-machining on the surface by Ga ion gun, *in-situ* after plating a thin protecting layer of platinum on the surface. The presence of porous structure within the bulk of the MPL is evident from the FIB images in Fig. 11b and c. By examining the cross-section of the GDL by SEM in Fig. 11d, the thickness of the MPL can be ascertained to be from 50 to 60 μm. In addition, the SEM image of the GDL cross-

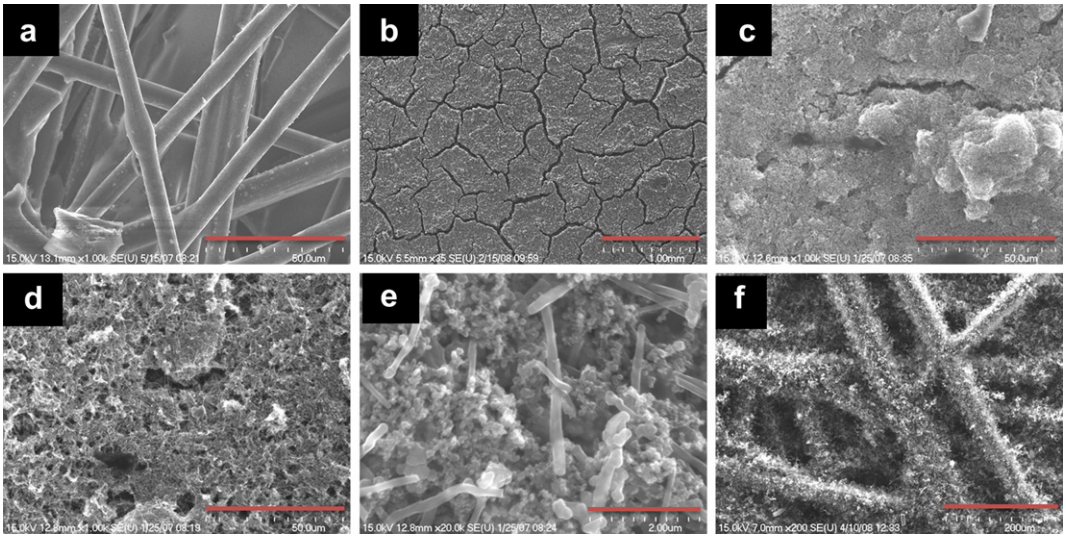

Fig. 9. Scanning electron micrographs of (a) non-woven carbon paper substrate, (b) and (c) MPL surface showing the mu-cracks at different magnifications, (d) and (e) MPL with homogeneous surface at different magnifications (f) GDL surface fabricated by using *in-situ* CVD on carbon paper.

section does not show any carbon bleed-through from the MPL to the uncoated side of the macro-porous carbon paper substrate.

2.1.8. Contact angle and surface energy

Surface energy defines the work required to enlarge the surface area of matter. When a droplet is placed on a surface, the contact angle is the angle formed between the outer edge of the liquid droplet and the solid surface. If the contact angle is 0°, the liquid completely wets a solid surface. A contact angle greater than 90° implies that the surface is resistant to wetting by the liquid in question. This is illustrated in Fig. 12a. The surface energy is related to the contact angle θ by Young's equation

$$\gamma^{sv} = \gamma^{sl} + \gamma^{lv}\cos\theta \quad (7)$$

where γ^{sv} is the solid surface free energy, γ^{sl} is the solid/liquid interfacial free energy, and γ^{lv} is the liquid surface free energy. In general, a liquid will wet a surface when the surface energy of the solid is larger than the surface energy of the liquid [76].

The methods described in this section determine the external contact angle of GDL materials with various chemical composition. Changes in PTFE content due to aging of the GDL can be detected by contact angle measurements. However, it is argued that the surface roughness of the GDL samples affects the contact angle more than the chemical composition of the sample. Since the external contact angle of pure PTFE to water is smaller than values observed on GDLs, the presence of the hydrophobic agent inside the GDL pores cannot explain the high contact angle values, but rather the contribution of the GDL surface roughness. Surfaces with a roughness above of approximately 1 μm generate higher contact angles to water than smooth surfaces. In general the external contact angle may describe only qualitatively the wettability of GDL materials it should not be used as a quantitative estimation for calculations or design purposes [77]. However, it is also possible to make rough corrections on the observed contact angles for the effects of the surface roughness [78].

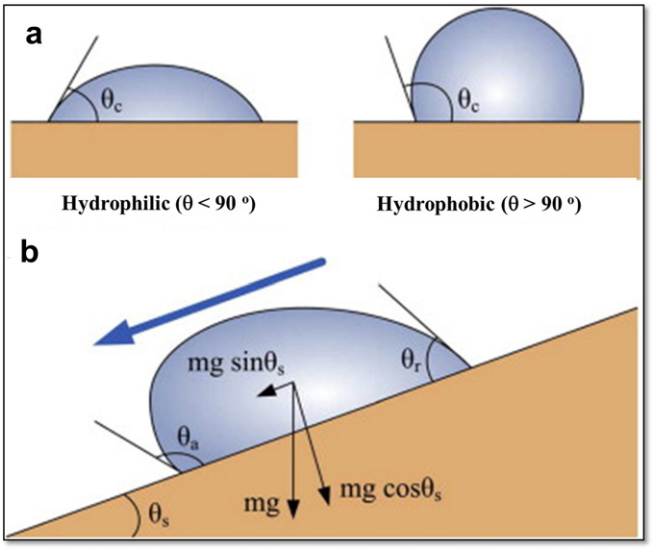

Fig. 12. Illustration of (a) the contact angle of hydrophilic and hydrophobic GDL surfaces and (b) the method of sliding angle as adopted from [85].

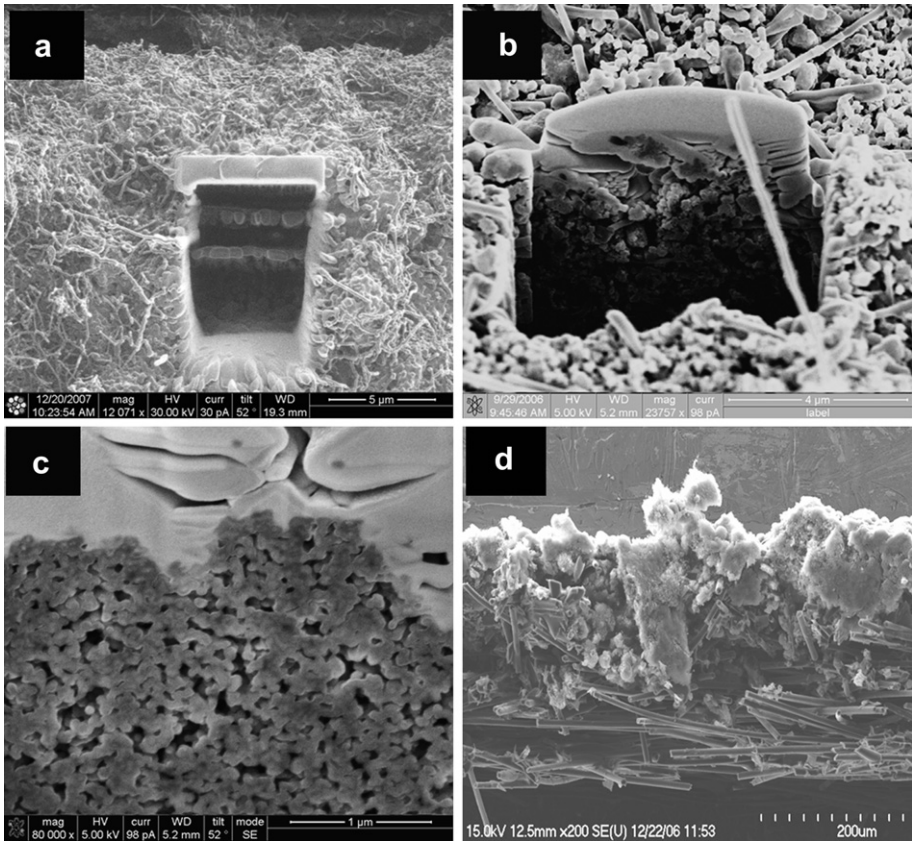

Fig. 11. Cross-section of MPL showing the presence of porous nature by FIB at (a) 12,000×, (b) ~24,000× and (c) 80,000× magnifications and (d) cross-section of GDL showing the carbon paper substrate and MPL.

An internal contact angle to water reflects a statistical average over GDL properties at the microscopic level. This measure can be obtained using the Washburn method [79] as described in [39] and [77]. The mass of liquid absorbed by the sample is recorded as a function of time through the computer interfaced with a microbalance. The Washburn constant in Lucas–Washburn equation [79] is first determined using *n*-hexane as wetting fluid, as its contact angle to GDL pores can be assumed to be zero. With Washburn constant of the GDL known, contact angles against four different wetting liquids can be measured using mass-squared-versus-time data and the Lucas–Washburn equation. Consequently, with this data and the known surface tension components of water, the internal contact angle of the GDL material to water can be calculated using the Owens-Wendt theory [80].

As a contrast to the external contact angles, all internal contact angles to water determined in [77] were less than the contact angle to water of pure PTFE, which can be considered as a proof of higher reliability of this method compared to conventional techniques measuring external contact angles. It was also stated that uncertainties within 3° for the contact angle to water can be obtained with this method when at least five test fluids are employed [77]. Although being quite laborious technique compared to simple external contact angle measurements, this method provides valuable quantitative information.

2.1.8.1. Sessile drop method. The most common method for measuring the external contact angle on a GDL is called sessile drop method. In this technique, a droplet of liquid is set on the GDL and the contact angle is measured by fitting a tangent to the three-phase point where the liquid surface touches the solid surface. This is most conveniently done by using a digital video camera and a computer program that can directly calculate the surface energy, if at least three different liquids have been used [81–83]. The drop size should be small in order to prevent influencing the contact angle by the weight of the drop itself, and the data should be recorded before significant evaporation [8]. Various forms of dynamic sessile drop methods exist. For instance, the fine movement of the contact angle due to the instability of the droplet can be recorded as a function of time. Alternatively, the plane on which the GDL sample is supported can be gradually tilted and the critical angle of tilt that causes the drop to draw away is recorded. This technique is referred to as sliding angle method, and is illustrated in Fig. 12b [84,85]. It is also possible to use a gradually increasing air flow to blow the droplet away [86].

2.1.8.2. Wilhelmy plate method. Another common technique for determining the contact angle is Wilhelmy plate method [50,87]. In this technique, a rectangular-shaped piece of GDL is dipped vertically into liquid. In a static version of this method, the sample is inserted a known distance and the force is measured. From the force it is possible to calculate the contact angle. In the dynamic version the GDL is dipped and removed at a constant rate as the force is monitored. This method allows for better statistics than the static version due to large number of observations. The method provides two separate characteristics of the wetting properties: advancing and receding angles related to the sample insertion and removal phases, respectively. The advancing angle displays the surface attraction for the liquid, and the receding angle reflects the surface repellency of the liquid [8].

The Wilhelmy plate method gives more reliable results than the sessile drop measurement. This is because the shape of the drop on rough surfaces in the sessile drop measurements can be affected by the surface texture, whereas in Wilhelmy plate method a larger three-phase boundary is examined. However, the drawback of the Wilhelmy plate method is that it can only be applied to materials having same properties on both sides, i.e. GDLs with micro-porous layer cannot be measured by Wilhelmy plate method directly. The solution is to attach two GDLs together so that the surfaces of interest are facing outside [8].

2.1.8.3. Capillary rise method. Capillary rise method is another technique used to determine the surface energy and contact angle of GDLs, as shown by Lim & Wang [58]. The height of the meniscus in a round glass tube having a known inner radius is related to the contact angle by the capillary law

$$\sin\theta = 1 - \frac{\Delta\rho g h^2}{2\sigma} \tag{8}$$

where θ is the contact angle, $\Delta\rho$ the difference between the densities of liquid and vapor, g the gravitational acceleration, h the meniscus height, and σ the liquid–gas surface tension of water. Therefore it is possible to calculate the contact angle from a meniscus height measured experimentally. In the study by Lim & Wang an optical technique to directly record and measure the capillary meniscus height was employed.

2.1.9. Cyclic voltammetry

Cyclic Voltammetry (CV) is used as an electrochemical technique for the characterization of electrodes and electrochemical reactions. In this technique, the voltage is swept between two values (V_1 and V_2) at a fixed rate. Starting from V_1, the voltage is increased to V_2 at the pre-fixed rate and on reaching V_2, the scan is reversed and the voltage is swept back to V_1. As the voltage is initially swept from V_1, the equilibrium at the electrode interface begins to change and current starts to flow. As the voltage is increased, the current raises from the initial value due to the electrochemical conversion of the electroactive species in solution resulting in a peak current. During the reverse scan, if the electrode reaction is perfectly reversible, the same electrochemical reaction occurs in the opposite direction thereby showing a peak current ideally of the same magnitude as in the forward scan. This aspect of CV can be exploited in the characterization of the reversibility of the GDL and thus serve as the *ex-situ* method. The featureless CV pattern of the GDL implies not only the reversibility of the GDL but also the absence of any electroactive impurity in its surface. CV is reported as a characterization technique for the GDL in acidic medium at room temperature [50,51]. The featureless CV pattern (without any redox peaks) of the carbon papers prepared at different carbonization temperatures is reported to be due to the absence of any electrochemical reaction on the surface of the electrode [50].

CV can also be employed in identifying the carbon corrosion occurring in the GDL upon cycling at high potentials. Speder [88] showed that when Pt black electrodes supported on a GDL were cycled at 0.45–1.6 V vs. RHE for 8 h, the resulting CV patterns revealed drastically increasing double-layer current and an obvious formation of redox peak at 0.55 V vs. RHE. This peak can be related to hydroquinone/quinone (HQ/Q) redox couple, $>C{=}O + e^- + H^+ \rightleftharpoons C{-}OH$, as also reported in [89]. According to Speder, the HQ/Q peak in the CV can also indicate the formation of other carbon surface oxides, such as phenols, lactones and carboxylic acids [88]. On the other hand, it is argued that the electrochemically active HQ/Q functional groups usually account for only a small fraction of the total surface oxygen generated during electrochemical oxidation of carbon [90].

2.1.10. Modeling and simulation

Computational modeling and simulation in GDL is a rapidly evolving area of research thanks to advancements in computing power. *Ex-situ* modeling of GDL materials focus on characterizing

the material properties without accounting for interactions with other fuel cell components. These models usually emphasize understanding gas and liquid transport through the GDL. Pore network and lattice-Boltzmann modeling methodologies have emerged as the most active areas of research and are described below [91,92].

2.1.10.1. Pore network models. The pore network model captures the essential physics and utilizes an idealized network to represent the porous structure of the GDL. Pore network models are frequently used to simulate the GDL in PEMFCs due to their numerical effectiveness. Some simulations were developed to study macroscopic static properties such as the capillary force as a function of water saturation [93,94]. More recently, pore network modeling has been focused on the study of water transport and two phase flow through the GDL [91,95–100].

In a pore network model, the porous medium is represented by a network of wide pores connected by constricted regions called throats [91,92], as shown in Fig. 13a. One side is the inlet face, where water is injected; the other side is the outlet face, connected to the gas phase. The geometrical parameters of pore network, such as pore/throat size, throat length, anisotropy, etc. can be retrieved from 3D volume imaging or a digitally constructed micro-structure using stochastic models [91]. The latter method has been mostly employed due to its low cost and high efficiency [91]. The constructed micro-structure will usually match the porosity obtained from experiments.

In typical pore network models of water transport [92,99], the GDL is initially fully filled with gas/wetting phase. The water/non-wetting phase is injected from the inlet side and displaces the gas. This two-phase transport is basically a drainage process. The water invasion pattern depends on primarily two parameters [92,101]. One is the ratio of dynamic viscosities of the two fluids (water/air here); the other is the capillary number *Ca*, the ratio of viscous force acting at the pore scale and capillary force. In particular,

$$Ca = \frac{v \cdot \mu_{nw}}{\sigma} \tag{9}$$

where v is the water velocity, μ_{nw} is the dynamic viscosity of water; σ is the surface tension. In a typical fuel cell application, the viscosity ratio and capillary number are ~ 17.5 and $\sim 10^{-8}$, respectively [92].

In such a small *Ca* number, the driving force for the flow is dominated by the capillary force. In the model, in order to have the water invasion to throats, the pressure difference across meniscus between water and air must surpass the capillary pressure, namely,

$$P_{H_2O} - P_{air} > P_c \tag{10}$$

where P_c is the capillary pressure as described in Eq. (3) with r_{min} referring to throat radius [92]. The pore connected to the filled throat will be invaded automatically due to its larger size. There will be laminar flow of water from one pore to the other pore if the pressure difference between these two pores is above the capillary pressure of throat that connects them. Following such a flow algorithms, the water will flow in a path with the least resistance, which can be theoretically visualized and studied. Fig. 13b gives an example for the evolution of the water front, which follows a simple capillary fingering pattern [92]. This pattern is favorable in applications, since many pores are not invaded and available for gas transport [99]. As further revealed by Sinha *et al.* [92], when *Ca* becomes larger (by increasing flow speed or decreasing hydrophobicity of GDL), the pattern will switch to compact invasion.

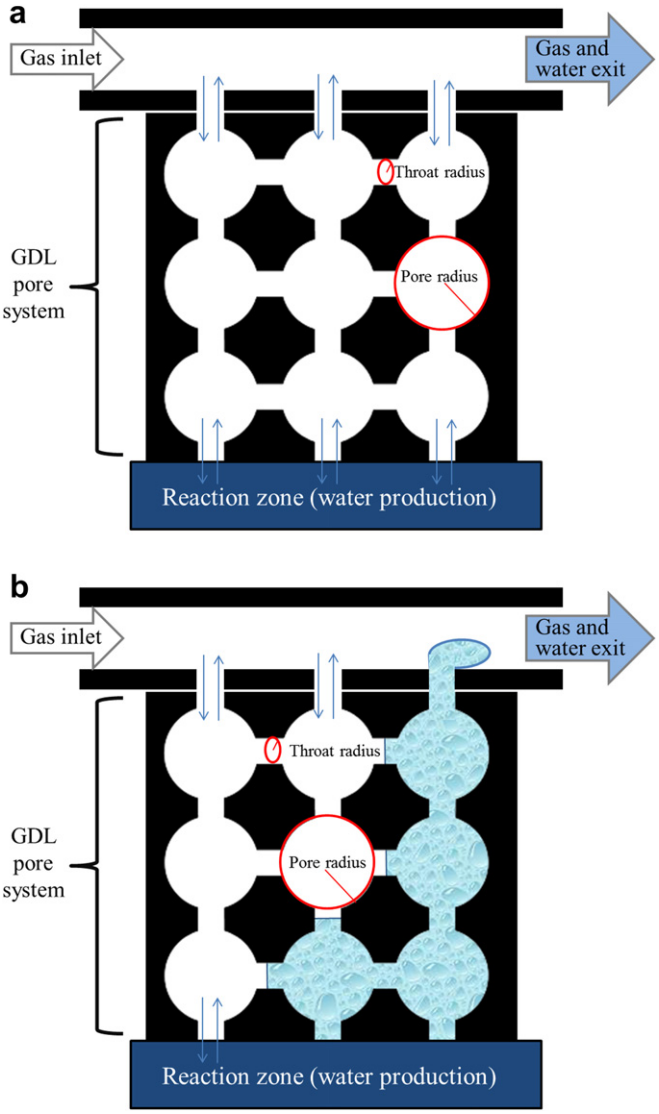

Fig. 13. Schematic of pore-throat network evolution (a) without water and (b) with water front, based on references [92,96].

For a compact pattern, the pores of GDL will be vastly occupied by water, therefore block the transport of gas and degrade the function of the fuel cell [99].

Due to its relative simplicity, the pore-network modeling has been widely implemented to study the water flow in GDL under different conditions, including mixed wettability [99], water nucleation in bulk [97] and incorporated micro-porous layer [96]. However, for the purpose of a more quantitative comparison with experimental results, more detailed but computationally expensive models based on lattice-Boltzmann and lattice gas, molecular dynamics, and computational fluid dynamics, incorporating a digitalized structure from actual porous medium and rigorous flow description, may have to be employed [91].

2.1.10.2. Lattice-Boltzmann models. In a lattice-Boltzmann (LB) model [102–104], the fluid is mesoscopically considered as a collection of fluid particles. The fluid medium is divided to a lattice network. The velocity of fluid particles is discretized, so the motion was allowed only between lattice points. If two particles meet at the same lattice point, then a collision will occur. For a GDL application, very typically a D3Q19 velocity discretized scheme is

employed as given in Fig. 14 [105]. In this scheme, the particles can move in 19 discrete velocities to the lattice points in the 3D lattice, including staying the same lattice point with the velocity (0,0,0).

Overall, the number density distribution of particles is evolved in the Boltzmann equation. The macroscopic properties of fluid such as density and velocity are obtained by average over a certain region of space [104,106]. These properties will have to comply with the Navier–Stokes equation for fluid, if an appropriate evolution of distribution function is established. Using different physical considerations of fluid, several LB based methods have been developed. Among them, two models have been received particular attention [107]. One is proposed by Shan and Chen [108] where the interaction between the neighboring fluid particles is described by an intermolecular potential. The other is the free energy model, proposed by Swift *et al.* [109]. In this model, the macroscopic properties such as contact angle and surface tension are introduced based on a solid physical sense [107]. Compared with pore network models, LB models treat the motion of fluid in a more realistic way and multiple fluid phases can be easily incorporated into the model. However, the LB model based calculations are also much more demanding on computational resources [91,104].

The application of LB model to study the transportation through GDL has increasingly evolved recently. For example, references [106,110] have simulated the effective diffusion and anisotropic permeability of GDL, which are in good agreement with experimental measurements. Hao *et al.* [107] have demonstrated that the liquid water can be removed more efficiently by the introduction of hydrophilic passages in the GDL.

2.1.11. Accelerated aging

There are many studies for catalyst durability evaluation, but very few of them address the durability of the GDLs. In general, during the operation of the PEMFC the GDLs become less hydrophobic leading to a reduction in gas convection and diffusion after lifetime testing [111]. Depending on the cell voltage, the carbon in the GDL could corrode/oxidize to CO or CO_2 in acidic environment leading to irreversible damage of PEMFCs. *Ex-situ* methods used for GDL accelerated aging under simulated PEMFC operating conditions are reviewed in this section.

The corrosion characteristics of the GDL were studied in a typical three-electrode cell setup as shown in Fig. 15 [112]. In order to simulate the PEMFC operating condition, the GDL was subjected to compression before testing with graphite board and a saturated calomel electrode (SCE) as the counter electrode and reference electrode, respectively in 0.5 M H_2SO_4 at 80 °C. The corrosion behavior of the GDLs was evaluated at 1.0, 1.2 and 1.4 V (vs. SCE) for 96 h using EG&G 263A potentiostat/galvanostat. The GDL samples were then examined for surface morphology by a color laser microscope (VK8550, Keyence, Japan), cross-section by SEM (JSM6360LV), in-plane resistances by four-probe method, wetting angle by water droplet method using goniometer and through-plane permeability by nitrogen gas flow method. The diffusivity, permeability, electrical resistivity, thermal conductivity, weight, thickness and the PTFE content of the GDL were severely affected during the accelerated durability testing.

Repetitive freezing followed by analyzing the pore size distribution, permeability, surface structure, and contact angle on the surface of a GDL were reported as one of the accelerated durability evaluation methods [113]. During the freezing process, the GDL was kept horizontal to make one side to have contact with water then frozen in a refrigerator at −20 °C. After 24 h, the cell was brought to room temperature to melt the ice completely and this procedure was repeated for 10 cycles. There was a significant reduction in porosity, enlargement of crack on the MPL surface, doubling of through-plane gas permeability and reduction in the contact angle due to the separation of PTFE from the carbon fiber after repeated freezing cycles.

The durability of the GDLs could also be evaluated by treating in 10% H_2SO_4 in water at 80 °C for 2000 h. It was observed that the hydrophobicity decreased continuously and flattened out after

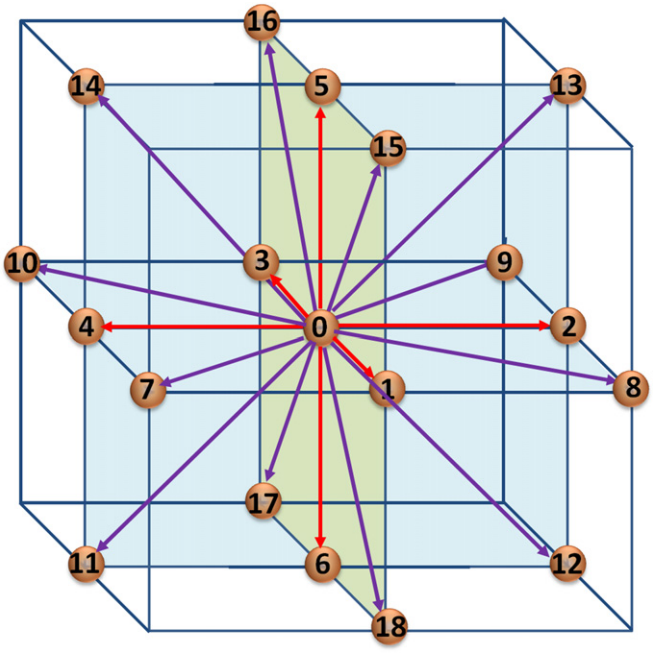

Fig. 14. Schematic of D3Q19 lattice structure as adopted from [105].

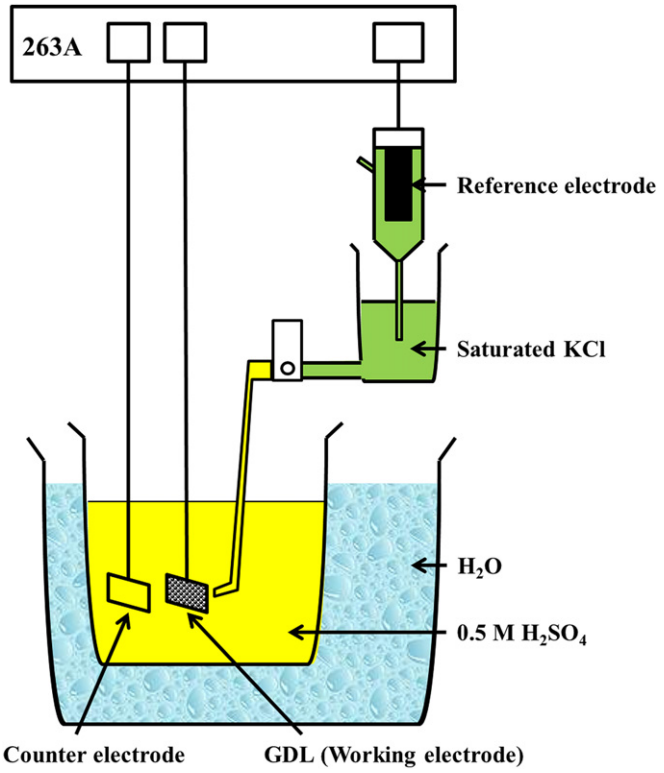

Fig. 15. Schematic of the three-electrode cell setup for electrochemical corrosion test as adopted from [112].

approximately 1000 h [114]. The carbon paper type GDL showed poor stability compared with carbon felt due to structural differences. It is interesting to note that the hydrophobicity loss of the GDL was caused by the carbon dissolution, as supported by TGA data, due to the structural degradation of carbonized resin. Fuel cell performance of the carbon felt type leached GDL showed about 80 mV voltage drop compared to fresh GDLs due to the loss of hydrophobicity. In another recent literature, GDL samples were aged in 0.5 M sulfuric acid by holding at 1.2 V vs. SCE for 100 h at 80 °C simulating PEMFC conditions [115]. Oxidation current exhibited by the carbon cloth based GDL was higher compared to that with carbon paper, probably due to the difference in degree of graphitization. This was also supported by the higher weight loss suffered by the carbon cloth based GDLs compared to that with carbon paper (3.7 vs. 1.8 wt. %).

2.2. In-situ methods

Even though the *ex-situ* methods are very important process control tools, *in-situ* methods are needed for understanding the GDLs under actual fuel cell operating conditions. GDL properties such as impedance, water transport, structural deformation, and durability can be examined by *in-situ* methods. These characterization techniques focus on measuring the effect of other components of the PEMFC on the GDL. The *in-situ* characterization of the GDLs can be conducted by assembling and studying the PEMFC single cells. The galvanostatic or potentiostatic polarization methods can be used to characterize GDLs at various RH conditions and temperatures using H_2/air in PEMFC single cells. In addition, the following *in-situ* techniques can be used to characterize the GDLs.

2.2.1. Impedance measurements

Impedance measurements are used for the characterization of electrodes and electrode reactions. Specifically known as Electrochemical Impedance Spectroscopy (EIS), this technique studies the response of the system to the application of a periodic small amplitude AC signal and the measurements are carried out at different frequencies. This technique is based on the principle that application of an electrical perturbation (current, potential) to an electrical circuit causes the appearance of a response. The response is resolved into the combination of electrical components such as resistance, capacitance and inductance, each of the components characterizing the physical or chemical phenomenon occurring at the electrode, electrolyte or interface. In the EIS, the interest is in the system response to the application of a sinusoidal signal such as,

$$E = E_0 \sin \omega t \tag{11}$$

where E_0 is the signal amplitude, $\omega = 2\pi f$ is the angular frequency, f is the alternating voltage signal frequency and t is time [116]. The ratio of the Laplace transforms of potential and current, $E(s)/i(s)$, is expressed in the units of resistance, Ω, and is called impedance, $Z(s)$. The Laplace transform is an integral transform in which a function of time $f(t)$ is transformed into a new function of a parameter s called frequency, $f(s)$.

In order to simplify the calculations of impedances, the result obtained for the periodic perturbation of an electrical circuit may be represented using complex notation where $j = \sqrt{-1}$.

$$E = E_0 e^{j\omega t} \tag{12}$$

and

$$I = I_0 e^{j(\omega t + \phi)} \tag{13}$$

Current and potential are rotating vectors in the time domain and these vectors rotate with a constant frequency, and the phase-angle (ϕ) between them stays constant. Instead of showing rotating vectors in time space it is possible to present immobile vectors in the frequency space, separated by the phase-angle. These vectors are called phasors and they are equal to $\tilde{E} = E_0$ and $\hat{\imath} = I_0 \exp(j\phi)$, where the initial phase shift of the potential was assumed to be zero [116].

In general the complex impedance may be written for any circuit by taking R for a resistance, $1/j\omega C$ for a capacitance and $j\omega L$ for an inductance, and applying Ohm's and Kirchhoff's laws to the connection of these elements [116]. In the case of a series connection of the resistance and capacitance, the impedance is given by

$$Z(j\omega) = R + \frac{1}{j\omega C} = R - \frac{j}{\omega C} \tag{14}$$

The result is represented graphically using two types of plots, namely complex plane or Nyquist plot, and Bode plot. The complex plane plot is a plot of Z'' (imaginary component) versus Z' (real component), plotted for various frequencies. In Bode plots, the graphs are made between log $|Z|$ (magnitude) and phase-angle (ϕ) versus log ω. In the case of a parallel connection of the resistance and capacitance, the impedance is given by

$$Z(j\omega) = \frac{1}{\frac{1}{R} + j\omega C} \tag{15}$$

Nyquist plots are the most often used in the electrochemical literature because they allow for an easy prediction of the circuit elements and they also allow for an easy relation to the electrical model. Total electrode impedance consists of the contributions of the electrolyte, the electrode–electrolyte interface and electrochemical reactions taking place on the electrode. Though the configurations and the characteristics of the electrodes give rise to different cases of electrochemical reactions, the one that occurs in the case of GDL of a PEMFC involves diffusion and adsorption in a porous electrode. Hence the impedance of Faradaic reactions in the presence of linear diffusion involving one adsorbed species (gas) at each electrode with a porous electrode model could be the ideal choice for the electrochemical analysis of GDL.

The total Faradaic impedance ($\hat{Z}_f$) consists of terms for $\partial i/\partial E$, $\partial i/\partial C_{0x}$, and $\partial i/\partial C_{\mathrm{Red}}$. The first derivative is called charge-transfer resistance (R_{ct}) and the other two are known as impedances of mass transfer or semi-infinite Warburg impedances ($\hat{Z}_{\mathrm{W,O}}$ and $\hat{Z}_{\mathrm{W,R}}$) [117].

Therefore,

$$\hat{Z}_f = R_{\mathrm{ct}} + \hat{Z}_{\mathrm{W,O}} + \hat{Z}_{\mathrm{W,R}} \tag{16}$$

For the ensemble of n pores and in the presence of the solution resistance outside the pores, the total impedance [118] becomes

$$\hat{Z}_{\mathrm{t}} = R_s + \frac{\hat{Z}_{\mathrm{por}}}{n} \tag{17}$$

where $\hat{Z}_{\mathrm{por}}$ is the total pore impedance. A literature survey on the application of EIS specifically to the study of GDLs of PEMFCs revealed that this technique is becoming one of the most dependable methods for characterization of electrodes, electrode components, and porous electrodes. Fig. 16 shows the impedance spectra of a fuel cell with three different GDLs at a typical operating potential of 0.55 V. Each semi-circle in the impedance spectra shows a particular process, the high frequency arc corresponds to charge-transfer process and the low frequency arc denotes the

diffusion process [1]. As the charge transfer occurs between the electrode and the electrolyte, the equivalent circuit of the electrochemical system contains the double-layer capacitance (C_{dl}) and charge transfer resistance (R_{ct}) in parallel for the kinetic controlled reaction. The diameter of the semi-circle in the Nyquist plot gives the value of R_{ct}. Left to right portion of the semi-circle denotes the high to low angular frequency. At the peak of the semi-circle, the angular frequency (ω) is related to C_{dl} as below, from which the C_{dl} value is determined and the equivalent circuit is developed.

$$\omega = \frac{1}{R_{ct} \cdot C_{dl}} \tag{18}$$

In a typical application of the impedance data, the effect of the PTFE content on the total resistance of the system along with the corresponding equivalent circuit (Fig. 17a) is reported [119]. PTFE content has been varied from 10 to 40% and its specific effect on the mass transport resistance (R_{mt}) is highlighted by the varying diameter of the second semi-circle standing for the mass transport resistance (Fig. 17b). For this system, the R_{ct} value remains almost constant for all cases of PTFE content variation, while the values of the capacitor (Constant Phase Element, CPE) and R_{mt} varied. Higher PTFE content increased the R_{mt} values. Hence, using the impedance spectra, types of resistances in the fuel cell array such as contact resistance, charge transfer resistance and mass transport resistance can be identified and corrective steps can be implemented.

Impedance has also been used to study the effect of compression and the role of the MPL in a PEMFC [120]. Three carbon cloth-based GDLs, one without MPL and two others with MPL were evaluated at two different clamping pressures (30 and 50%). The polarization resistance (R_p) and diffusion resistance (R_d) obtained at varying current densities (0–0.87 A cm^{-2}) and at two different temperatures (60 and 80 °C) highlighted that higher compression ratio (CR) decreased ohmic resistance but increased mass transfer and polarization losses. It was found that increasing the CR from 30 to 50% caused the worsening of cell performances due to the fact that higher CR increased mass transport resistance especially at high CD when the need for the reactants is maximum and thereby slowing down the kinetics of the electrode reaction. The presence of the MPL on the carbon cloth was extremely beneficial for the operation, especially at high current density, as it reduced the high frequency resistance of the overall assembly. The presence of the MPL on the

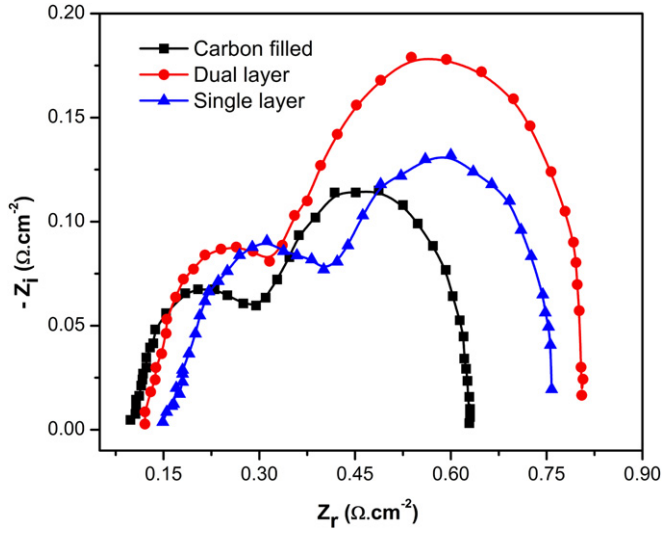

Fig. 16. Impedance plots of MEAs with three different GDLs using with H_2/air at 0.55 V [1].

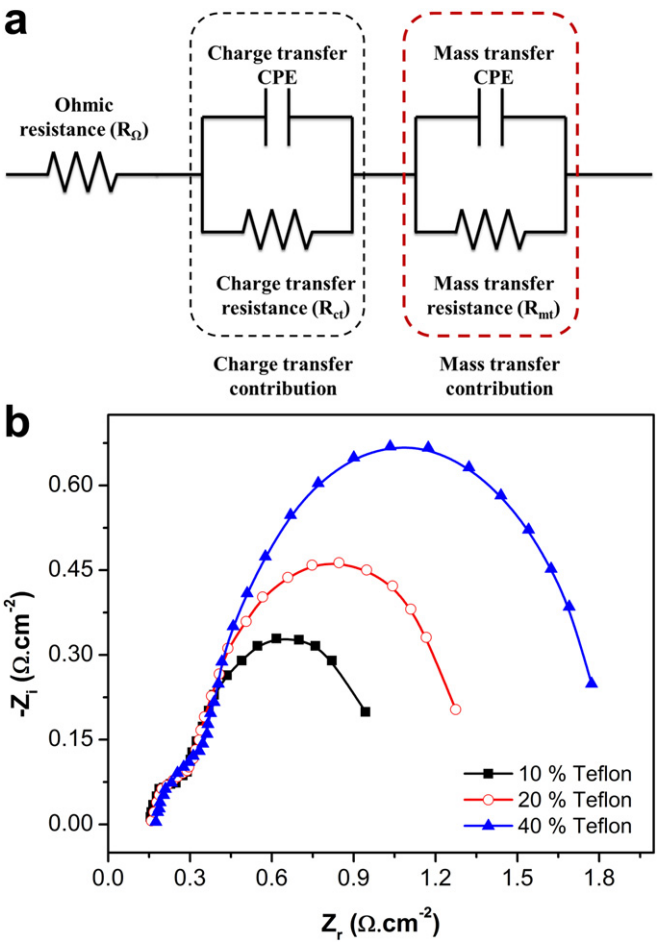

Fig. 17. (a) Equivalent circuit for an MEA showing charge and mass transfer components and (b) impedance spectra of MEAs with GDLs containing different Teflon contents [119].

carbon cloth was extremely beneficial for the operation, especially at high current density, as it reduced the high frequency resistance of the overall assembly.

A comparative impedance study of a carbon paper (woven-non-woven (WNW)) and a carbon cloth substrate at different current densities [121] revealed that the WNW substrate was superior to the carbon cloth in a vast range of current densities (from 0 to 0.8 A cm^{-2}). However, while at high current density, the WNW GDL had problems in water management. EIS was also used to investigate the charge transfer and mass transport properties of a Pt/carbon nanotube (CNT) based electrode. The authors reported that the *in-situ* grown CNT layer could provide both enhanced charge transfer and mass transport properties for the Pt/CNT based electrode [122] as an integrated GDL and CL in comparison with previously reported Pt/CNT based electrodes with a Vulcan XC-72R based GDL and a Pt/CNT based CL. Impedance spectra have been used to diagnose the variations in ohmic resistance, charge transfer resistance, and mass transport resistance with compression ratio [123]. The results showed that the optimal PTFE content, at which the maximum peak power density occurred, was about 5 wt.% for a GDL without an MPL coating, while for a GDL with an MPL coating, the optimal PTFE content in the MPL was found to be 30 wt. %.

EIS study has been used for the evaluation of freeze-dried macro-porous solid foams prepared from the multi-walled carbon nanotube (MWCNT) aqueous suspensions dispersed by chitosan

[124]. Thin film shaped CNT solid foams, prepared and applied to the GDLs of a laboratory scale PEM was reported to be advantageous for reducing the ohmic resistance in PEMFC assembly. A comparative study of CNT-GDL and Toray GDL has been carried out by EIS [125]. The authors reported that the cell with CNT-GDL had better electrical conductivity and mass transfer ability than those of Toray GDL. As a result, the limiting current density and peak power density of a direct methanol fuel cell (DMFC) with CNT-GDL were improved by 40 and 27%, respectively.

The electrochemical durability of a GDL under simulated PEMFC conditions has been reported [126]. Electrochemical oxidation of the GDLs was studied by potentiostatic measurements up to 96 h. The electrochemical impedance spectra measured at 1500 mA cm^{-2} was shown to imply that the ohmic resistance, charge transfer, and mass-transfer resistances of the fuel cell changed significantly due to corrosion at high potential. The higher hydrophobic property of GDL with CNT on carbon fiber with covalently assembled metal nanocatalysts was diagnosed by EIS [127] and implied self-humidification of PEMFC.

EIS study was used to evaluate the mass transport ability of diffusion layer in DMFCs. A high-water-discharge gas diffusion backing layer (HBL) of the cathode for DMFCs had been prepared by means of spreading diluted PTFE solution on one-side of carbon paper and heat treatment at 340 °C for 30 min [128]. EIS of DMFC with HBL proved better mass transport ability and a higher single cell performance at 60 °C.

The effective ionic conductivity of an electrolyte-soaked GDL had been carried out by EIS study from which the effective diffusivity [129] has been inferred. The effect of the hydrophobic agent and Nafion loading on the properties of the carbon fiber GDL was deduced with the help of EIS study [130]. The reduction of O^{2-} in 0.1 M H_2SO_4 on various uncatalyzed carbon fiber papers (two-electron process) was chosen as the additive-sensitive electrochemical reaction. The oxygen electro-reduction on the carbon fiber paper was shown to be a strong function of PTFE and Nafion content, as revealed by cyclic voltammetry and EIS. Thus EIS has been defined also as a quantitative technique as the changes in charge-transfer resistance could be used as a quantitative measure of both PTFE and Nafion content. The addition of PTFE increased the R_{ct} of the two-electron reduction (O^{2-}) as determined by impedance spectroscopy while the presence of Nafion decreased R_{ct}.

The EIS technique has seen immense increase in popularity in recent years. The technique, which was initially applied to the determination of the double-layer capacitance is now applied to the characterization of electrode processes and complex interfaces. Recent research also proves this technique to be both qualitative and quantitative.

2.2.2. Water transport visualization

The most simple and cost-effective way to visualize liquid water flow is by using transparent fuel cells as shown in Fig. 18 [131–133]. Typically, end plates and flow field plates, the support compressing inner fuel cell components together, are made from metal and graphite which are opaque to visible light. Substituting the opaque materials with transparent ones is a straightforward solution. However, most of the transparent materials are not electrically conductive, so transparent materials require special accommodation for current collection. The most common practice is to combine graphite gas channel ribs with transparent window (e.g. polycarbonate or plexiglass), which allows view to gas channels, but leaves the land areas out of view. With transparent fuel cells, spatial and temporal resolution is completely determined by the optics and recording equipment (CCD camera) as there is no limitation due to other parts of the equipment [134].

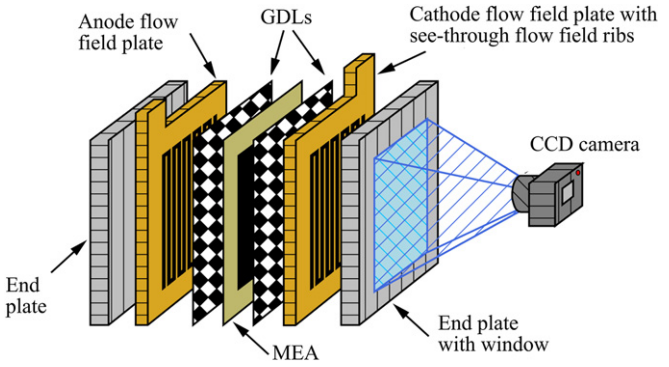

Fig. 18. Experimental apparatus with transparent cell for visual observations as adopted from [136].

So far, transparent fuel cells have been extensively used in water transport characterization [131–133]. Most of the research has focused on flow field design and optimization on cathode side, where the most problems with water removal evidently arise [131]. Some investigations also focus on the effect of GDL on the water removal characteristics [135,136]. This method only gives information on water content already removed from GDL, but nevertheless it provides an easy method to indirectly evaluate how different GDL materials perform with water management. An interesting option for the conventional method is to place a transparent window so that cross-sectional water profile can be visualized [137]. In addition, transparent fuel cells have been used in conjunction with other in-situ methods including pressure drop monitoring [134,136] and water vapor sensitive paper [138]. IR-imaging is also a useful addition as long as the window is also transparent within the infrared range [137,139].

2.2.2.1. Neutron imaging. Neutron imaging was first demonstrated for fuel cell research in 1999 by R. J. Bellows *et al.* [140], and rapid development has occurred since, making neutron imaging a well-established and frequently used method for studying water distribution in operating fuel cells [141]. To date, neutron imaging is also the only *in-situ* method that yields condensed water distribution information from commercial grade fuel cells without the need of heavy modifications on the original design [142]. Neutron imaging is based on different neutron attenuation properties between elements. As neutrons carry no electrical charge, their interaction with matter is restricted to the atomic nucleus, that is, the interaction between neutrons and matter is dominated by strong nuclear force [143]. A neutron colliding with a nucleus can either be absorbed or scattered. Most materials only scatter neutrons, but due to the complex interactions on the nuclear level, elements with similar number of nuclei might have completely different attenuation characteristics [141,142]. Hydrogen and hydrogen-containing materials like water, plastics, and oil strongly attenuate neutrons while neutrons easily pass through steel, aluminum, and carbon [143,144]. Compared to liquid water however, neutron attenuation due to water vapor and gaseous hydrogen is negligible owing to their over two magnitudes lower atomic density. So taken that, except for water, all other heavily neutron scattering materials are eliminated, neutron imaging enables clear visualization of water content on an operating fuel cell.

In conventional neutron imaging equipment (see Fig. 19), a neutron beam is transmitted through the sample and the attenuation image is recorded by a neutron detector, usually a scintillator screen combined to a CCD camera [141,143]. The high resolution needed for fuel cell and in particular GDL imaging requires high flux

neutron beams available only from nuclear reactors or particle accelerators (neutron spallation). Due to the high cost, there are only few suitable neutron imaging facilities worldwide. These include NIST Center for Neutron Research (CNR), USA [142–144], Penn State Radiation Science and Engineering Center, USA [145], Paul Scherrer Institute (PSI), Switzerland [146,147] Helmholtz-Centre, Germany [148,149], and Korea Atomic Energy Research Institute [150], to name a few. The state of the art facilities are capable of spatial resolutions of 20 μm, but typically the resolution is around 100–150 μm [133,141,151]. The time taken to record one image depends on the neutron flux intensity and is usually in the order of few seconds [133,141]. In contrast to visual imaging, neutron imaging also provides quantitative information of the thickness of water layers [142].

In fuel cell neutron radiography, two different viewing directions are usually considered, through-plane and in-plane. Through-plane neutron imaging characterizes water content along electrochemically active area and it has been extensively used to study various flow field and GDL effects on the fuel cell water management and performance [145,146,149,152–156]. Through-plane imaging gives a clear visualization of liquid water accumulation within the flow channels, but it also gives some info on the water content in GDLs and MEA [152]. However, it is impossible to distinguish how the water is distributed between overlapping areas along the beam direction. For instance, differentiation between anode and cathode side water content would need a specially designed fuel cell with non-overlapping flow fields [152]. Most of the through-plane imaging research focuses on flow field optimization, but some papers have studied the effect of different GDLs on the water balance [152,153]. Through-plane neutron imaging was also successfully used in conjunction with current density [157] and humidity [154] mapping. Another option is to orient the neutron beam to in-plane direction, which gives data on how water is distributed along the different components of fuel cell [142]. For in-situ testing of GDLs, this method provides very useful information on the membrane hydration, water accumulation on GDLs and flow channels, and on the interfaces of these components [142]. So far, in-plane imaging has been primarily done at NIST-CNR and PSI because of the high resolution requirements [142,144,147,158].

Neutron tomography has been demonstrated with fuel cell water imaging, but several radiographies need to be recorded by each tomogram and the measurement times are in the range of several hours [135,141,148]. As the water distribution in an operating fuel cell changes in the matter of seconds, the only way to get a useful image was to stop the gas flows during the tomography [148]. Recent developments in tomogram reconstruction algorithms and neutron image intensifiers have shown good progress [159,160]. Tomogram measurement times of 15 s at 107 μm resolution were demonstrated with a 3-cell PEMFC stack, but the method has not yet been used for *in-situ* testing [160].

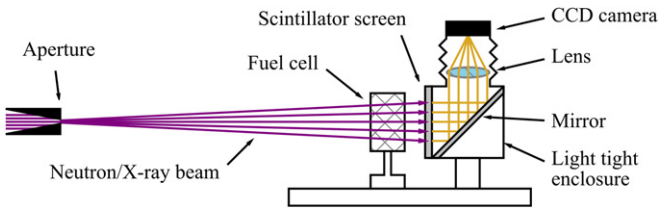

Fig. 19. Experimental setup for fuel cell imaging by radiation attenuation as adopted from [144].

2.2.2.2. X-ray imaging. The principles of X-ray imaging do not differ much from neutron imaging as X-ray imaging also relies on the fact that materials have different attenuation coefficients. X-ray photons interact with the electronic shell of atoms and the attenuation comprises numerous effects: photoelectric attenuation, Rayleigh scattering, Compton scattering and electron–positron pair production [141]. X-ray attenuation coefficients increase consistently with the atomic shell electron number [144]. Due to the relatively low X-ray attenuation characteristics of water, it had been thought that X-ray imaging would not be suitable for water content visualization in fuel cells containing metal and carbon components [161]. However, with sufficiently low X-ray energies (<50 keV "soft X-ray"), sensitivity to water is greatly enhanced [162,163]. But even though, thick metal end plates cause trouble with their high X-ray attenuation, and perforations in the metal plates or non-metallic components are necessary for high contrast images [151,162].

On commonplace X-ray equipment, X-ray tubes are used to accelerate electrons which hit a target to produce a broad spectrum of X-ray energies surpassing 100 keV [141,161]. However, the low energy X-ray beams necessary for water imaging are only available in certain synchrotron facilities at Helmholtz-Centre Berlin [151,162,164] and Spring-8 in Japan [163]. Compared to conventional X-ray tubes, synchrotron X-ray beam provides several orders of magnitude higher flux, which allows very fast measurements, in the order of milliseconds. Attenuation coefficients do vary with photon energy so a monochromatic beam would enable better quantification with specific energy attenuation coefficients [141]. The spatial resolution can reach 3 μm with a monochrome beam [151]. As with neutron imaging, the X-ray detection is based on scintillator screens combined to a CCD camera.

The high spatial and temporal resolution allows through-plane X-ray imaging to visualize the eruptive water transport mechanism from GDL pores to flow channels [151,162]. In-plane X-ray imaging also provides enough resolution to observe the water content in MPL [164]. The comparatively fast measurement times make X-ray imaging suitable for 3D tomography. Kruger *et al.* [165] designed a setup which took 1800 angle projections over 60 min to form a tomogram with 10 μm voxel resolutions. Although synchrotrons are the main source of X-rays for fuel cell imaging, commercial X-ray tube light sources have been successfully used to study liquid water accumulation in the flow channels [166]. This gives promise of easier access to fuel cell compatible X-ray imaging facilities. The main drawback is that in all the cases above, the fuel cell itself had to be specially designed to minimize X-ray attenuation due to metallic components.

2.2.2.3. Nuclear magnetic resonance imaging. In nuclear magnetic resonance (NMR) imaging (MRI) specific atomic nuclei with non-zero spins are excited by radio-frequency pulses in the presence of a strong magnetic field. The excited nuclei absorb this radio signal and resonate at a frequency proportional to the applied magnetic field strength [133,167]. The presence of water molecules can be detected by recording signals emitted by excited hydrogen nuclei [133]. The radio-frequency pulses are created by a coil aligned perpendicular to the magnetic field and the resulting signal is recorded with a receiver coil. Similar to X-ray imaging, MRI has been used in a wide array of medical applications. However, fuel cell MRI requires some modifications to the cell design: current collection needs to be done without ferromagnetic materials and the amount of electrical conductors need to be held at minimum due to eddy currents inflicted by the strong magnetic field [167]. MRI has been applied very successfully for investigation of small fuel cells, although finding suitable non-metallic heating components can be an issue [151,161]. The spatial resolution of current equipment is from 50 to 200 μm and temporal resolution is usually

in the order of minutes, but these are subject to change as only preliminary work has been done for optimizing the radio-frequency pulse signals for fuel cell water content imaging [133,167]. GDLs are good electrical conductors that shield electromagnetic waves making it impossible to use MRI to monitor the water distribution within the GDL [161]. Nevertheless, MRI does allow water content visualization on the electrolyte membrane and flow channels.

2.2.3. Modeling and simulation

In-situ modeling and simulation of the GDL involves modeling the interaction of the GDL with other fuel cell components. These simulations usually include a complete fuel cell system and generate overall system performance predictions such as polarization curves. The most common approach to fuel cell system modeling involves computational fluid dynamics (CFD).

CFD modeling uses a numerical approach to solving a family of coupled non-linear equations for fluid flow. The relevant fuel cell system components will be modeled then decomposed into a large number of finite volume elements. Each finite volume element is characterized by a set of bulk material properties and relevant fluxes are calculated through the boundaries of that element. The values used to characterize each volume element can be the result of measurements of material properties or other simulations. The basis for these simulations are a set of conservation equations for mass continuity, momentum, energy, chemical species, water content, and electric and ionic potential [168]. These fundamental conservation equations describe the flow of materials such as liquids, gasses, and charged particles through the flow field, GDL, catalyst layers and membrane. They are supplemented with equations specific to the particular materials within the system and can include spatial and temperature dependencies. The complexity of the equations involved and the large number of boundary conditions require that the equations be solved numerically [91].

One of the major challenges of *in-situ* modeling is accurately characterizing the behavior of the GDL without modeling the micro-structure. Including a detailed micro-structure for an operational fuel cell would be far too computationally demanding. One approach to overcoming this difficulty has been the use of multi-scale models [169]. However, most CFD models will approximate the GDL by assigning effective macroscopic properties. These properties can vary spatially within the system but the degree of detail must remain relatively coarse in order to maintain reasonable computational times. The macroscopic GDL properties such as porosity, gas diffusion constants, and water transport characteristics will be determined experimentally or by using the results from micro scale models like pore network or lattice-Boltzmann.

Many *in-situ* models focus on the effects of GDL deformation due to compression. Deformation will cause the GDL to intrude into the channel which has a major impact on fuel cell performance [32,170,171]. It was also found that GDL materials need to be highly uniform or the effects of intrusion will cause significant performance variation between different cells made with the same batch of material. Compression also changes the porosity which affects gas and water flow [172–174]. The most common approach involves using a structural model to predict the deformation of the GDL. The structural model uses mechanical parameters and relates them to properties which are altered by compression such as porosity and electrical conductivity by using theoretical predictions and experimental measures. Some of the earliest models used simple linear relations between thickness and porosity [172], which improved performance predictions compared to models which ignored deformation effects. Models for GDL deformation have been improving and one of the latest developments is a non-linear orthotropic model by Garcia-Salaberri *et al.* [175]. This model

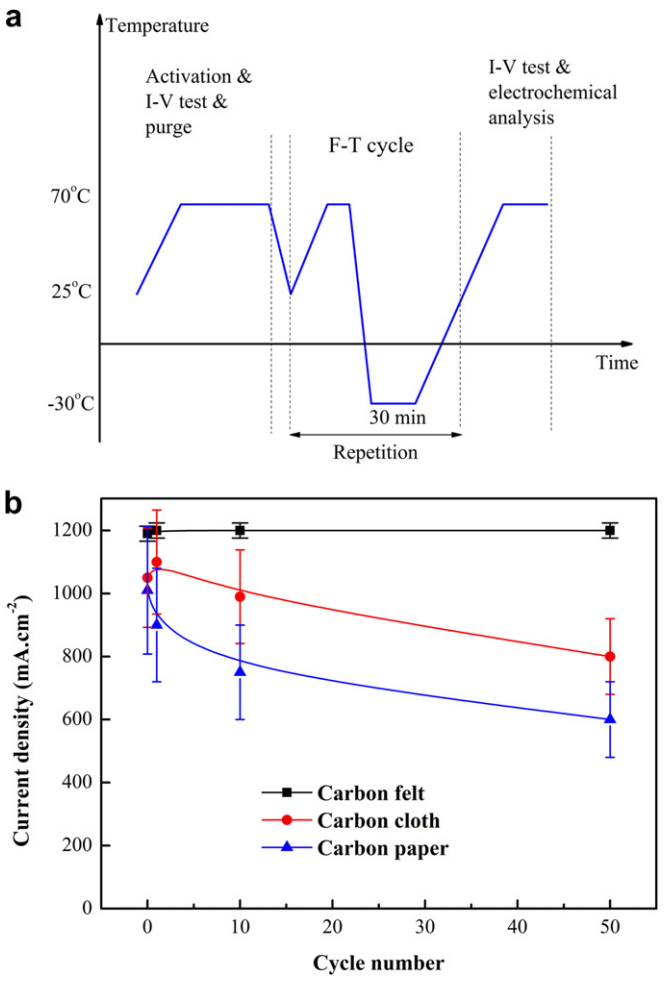

Fig. 20. (a) Accelerated freeze-thaw durability profile and (b) performance degradation of carbon paper, felt and cloth based GDLs as adopted from [177].

produces a much more detailed relationship between mechanical properties and the resulting physical changes such as intrusion into the flow channel and contact pressure. Accurate contact pressure predictions are necessary for determining the expected thermal and electrical contact resistances between the GDL and channel ribs, which are important performance parameters [9,22]. Advanced structural deformation models coupled with computational fluid dynamics are powerful analytical tools for characterizing the performance of the fuel cell and the interaction between the GDL and other fuel cell components.

2.2.4. Accelerated aging

Automotive application requires the PEMFC to support cold start at −20 °C and survivability at −40 °C as specified by U.S. Department of Energy (DOE). The presence of water within the pores of the GDLs could cause mechanical stress during the freeze/thaw operation of the PEMFC. It is observed that the carbon paper based GDL shows faster performance degradation to that with carbon cloth on freeze-thaw cycling between −40 and 80 °C [176]. Lim *et al.* [177] conducted freeze-thaw durability of carbon paper, carbon felt, and carbon cloth based GDLs in the PEMFCs with −20–70 °C as shown in Fig. 20a, and monitored the fuel cell performance after 50 cycles. The performance degradation was negligible for carbon felt based GDLs during freeze/thaw cycling conditions as seen in Fig. 20b. In addition, the GDLs were also analyzed by SEM and impedance studies.

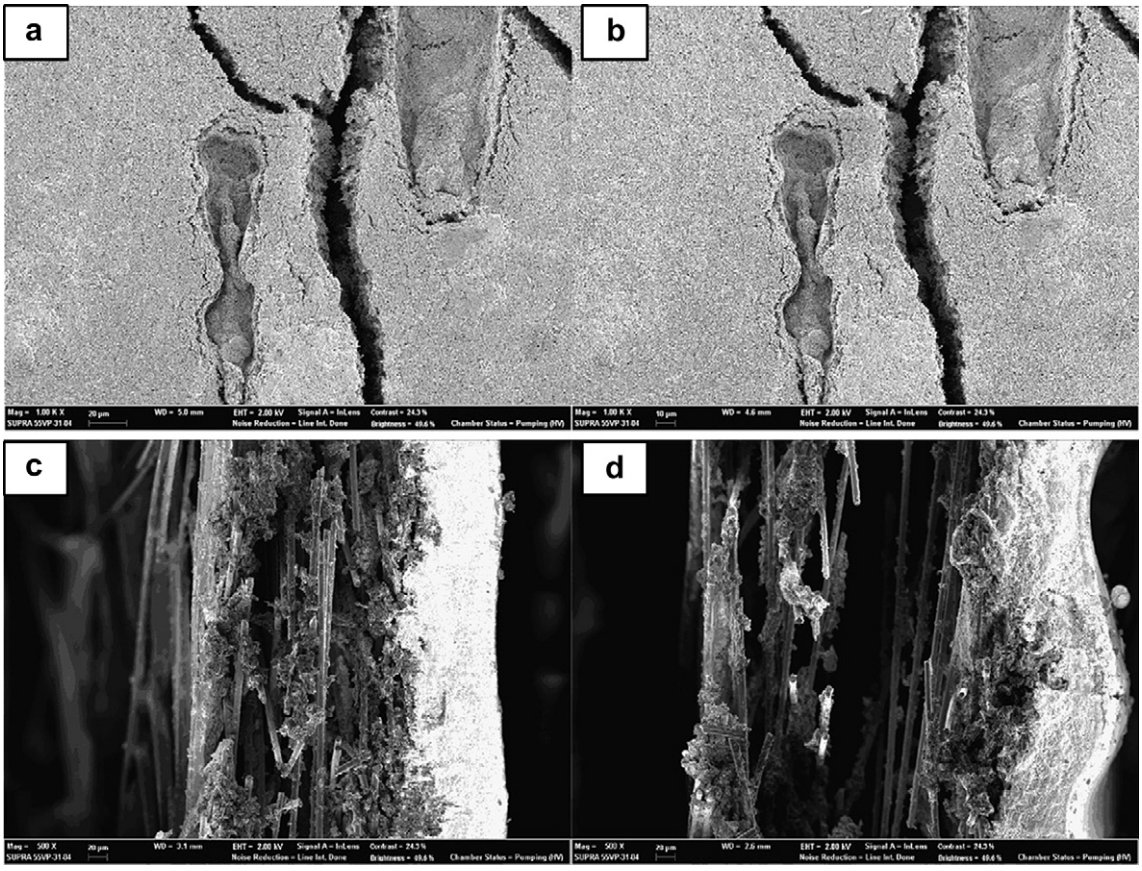

Fig. 21. Surface morphology of the MPL (a) before and (b) after the corrosion test and the cross section of the GDL (c) before and (d) after the corrosion test at 1.45 V [41].

An accelerated carbon corrosion of the GDL (25 cm^2) was conducted with an external voltage of 1.45 V with humidified gases (air (1000 SCCM) and H_2 (300 SCCM)) at 65 °C in a PEMFC for 96 h. 100 h at 1.45 V is conceived to represent 5 years of automotive fuel cell use due to carbon corrosion [41]. Pt mesh was placed between the CL and cathode GDL to prevent adhesion of the MPL with the CL. With this cell configuration, changes in thickness, weight, surface morphology, pore size, air permeability and fuel cell performance could be monitored after the accelerated corrosion testing. Fig. 21a and b show surface morphology of the MPL before and after the corrosion test at 1.45 V. Evidently, the shapes of the holes, cracks, and scratches the MPL remain unaltered indicating that the carbon corrosion does not affect the MPL surface layer. Fig. 21c and d show the cross-section of the GDL before and after the corrosion test. The accelerated durability test corroded the center of GDL with a large gap leading to structural weakness.

3. Conclusion

GDLs form an integral part of the MEA for PEMFCs by performing several important functions including transportation of reactants to and from the reaction sites. The material properties and structural characteristics of the substrate and the MPL strongly influence the fuel cell performance. This review groups together the set of tools for GDLs evaluation by *ex-situ* and *in-situ* methods. In particular, properties such as electrical conductivity, thermal conductivity, porosity and pore size distribution, surface energy, wetting characteristics, cross-section morphology, modeling and simulation have been identified and discussed using *ex-situ* techniques under simulated PEMFC conditions. In addition to these properties, impedance spectroscopy and imaging techniques have also been discussed as *in-situ* methods. A wide range of accurate and well understood characterization techniques are crucial for developing high performance and durable GDLs for automotive and stationary applications. In this context, *ex-situ* methods are the most important tools for GDL manufacturers around the world. However, exactly simulating the fuel cell stack operating conditions for GDL characterization by *ex-situ* techniques is a major challenge. Evidently, one has to employ both the *ex-situ* and *in-situ* methods for understanding and developing high performance GDLs for PEMFCs.

Acknowledgment

AMK would like to thank Fulbright Specialist program, US Department of State as well as VTT, Finland for financial support for visiting Tampere University of Technology and VTT, respectively during fall 2011. Funding by Finnish Funding Agency for Technology and Innovation TEKES is also acknowledged.

References

[1] M. Han, J.H. Xu, S.H. Chan, S.P. Jiang, Electrochim. Acta 53 (2008) 5361–5367.
[2] L.R. Jordan, A.K. Shukla, T. Behrsing, N.R. Avery, B.C. Muddle, M. Forsyth, J. Power Sources 86 (2000) 250–254.
[3] Z. Qi, A. Kaufman, J. Power Sources 109 (2002) 38–46.
[4] L.R. Jordan, A.K. Shukla, T. Behrsing, N.R. Avery, B.C. Muddle, M. Forsyth, J. Appl. Electrochem 30 (2000) 641–646.
[5] M. Neergat, A.K. Shukla, J. Power Sources 104 (2002) 289–294.
[6] S. Park, J.-W. Lee, B.N. Popov, Int. J. Hydrogen Energy 37 (2012) 5850–5865.
[7] L. Cindrella, A.M. Kannan, J.F. Lin, K. Saminathan, Y. Ho, C.W. Lin, J. Wertz, J. Power Sources 194 (2009) 146–160.

[8] M. Mathias, J. Roth, J. Fleming, W. Lehnert, in: W. Vielstich, A. Lamm, H.A. Gasteiger (Eds.), Handbook of Fuel Cells, Fundamental Technology and Applications: Part 1, Vol. 3, John Wiley & Sons Ltd, West Sussex, 2003, pp. 517–537.
[9] M.S. Ismail, T. Damjanovic, D.B. Ingham, M. Pourkashanian, A. Westwood, J. Power Sources 195 (2010) 2700–2708.
[10] S.M. Sze, K.K. Ng, Physics of Semiconductor Devices, third ed. John Wiley & Sons, Hoboken, New Jersey, 2007, 30–31.
[11] S. Yoshimoto, Y. Murata, K. Kubo, K. Tomita, K. Motoyoshi, T. Kimura, H. Okino, R. Hobara, I. Matsuda, S. Honda, M. Katayama, S. Hasegawa, Nano Letters 7 (2007) 956–959.
[12] American Society for Testing Material Committee, ASTM C611 – 98 (2010) e1 Standard test method for electrical resistivity of manufactured carbon and graphite articles at room temperature, ASTM International, West Conshohocken, PA, 2010.
[13] E-TEK, BASF Fuel Cell, Inc. [Online] Available: http://www.jonnycoder.net/aces/inside/index.php. [Accessed: 02/02/12].
[14] CeTech - Carbon Paper: Sheet type, 2007. [Online] Available: http://www.ce-tech.com.tw/english/GDL-03.html. [Accessed: 16/11/11].
[15] FuelCellsEtc. [Online] Available: http://fuelcellsetc.com/index.php. [Accessed: 20/01/12].
[16] M.V. Williams, E. Begg, L. Bonville, H.R. Kunz, J.M. Fenton, J. Electrochem. Soc. 151 (2004) A1173–A1180.
[17] J. Kleemann, F. Finsterwalder, W. Tillmetz, J. Power Sources 190 (2009) 92–102.
[18] L.J. Van der Pauw, Philips Res. Rep. 13 (1958) 1–9.
[19] J. Li, E.S. Steigerwalt, S. Sambandam, W. Lu, C.M. Lukehart, Chem. Mater. 19 (2007) 6001–6006.
[20] C. Kasl, M.J.R. Hoch, Rev. Sci. Instrum. 76 (2005) 033907.
[21] S.G. Kandlikar, Z. Lu, App. Thermal Eng. 29 (2009) 1276–1280.
[22] N. Zamel, E. Litovsky, X. Li, J. Kleiman, Int. J. Hydrogen Energy 36 (2011) 12618–12625.
[23] N. Zamel, E. Litovsky, S. Shakhshir, X. Li, J. Kleiman, Appl. Energy 88 (2011) 3042–3050.
[24] O. Burheim, P.J.S. Vie, J.G. Pharoah, S. Kjelstrup, J. Power Sources 195 (2010) 249–256.
[25] E. Sadeghi, N. Djilali, M. Bahrami, J. Power Sources 196 (2011) 3565–3571.
[26] American Society for Testing Material Committee, ASTM E2584-07 Standard Practice for Thermal Conductivity of Materials Using a Thermal Capacitance (Slug) Calorimeter (SUPERSEDED), ASTM International, West Conshohocken, PA, 2007.
[27] American Society for Testing Material Committee, ASTM E2584-10 Standard Practice for Thermal Conductivity of Materials Using a Thermal Capacitance (Slug) Calorimeter, ASTM International, West Conshohocken, PA, 2010.
[28] American Society for Testing Material Committee, ASTM D5470-06(2011) Standard Test Method for Thermal Transmission Properties of Thermally Conductive Electrical Insulation Materials, ASTM International, West Conshohocken, PA, 2011.
[29] G. Karimi, X. Li, P. Teertsra, Electrochim. Acta 55 (2010) 1619–1625.
[30] I. Nitta, O. Himanen, M. Mikkola, Fuel Cells 8 (2008) 111–119.
[31] M. Hamour, J.P. Garnier, J.C. Grandidier, A. Ouibrahim, S. Martemianov, Int. J. Thermophys. 32 (2011) 1025–1037.
[32] S.G. Kandlikar, Z. Lu, T.Y. Lin, D. Cooke, M. Daino, J. Power Sources 194 (2009) 328–337.
[33] K. Han, B.K. Hong, S.H. Kim, B.K. Ahn, T.W. Lim, Int. J. Hydrogen Energy 35 (2010) 12317–12328.
[34] M.S. Ismail, A. Hassanpour, D.B. Ingham, L. Ma, M. Pourkashanian, Fuel Cells 0 (2012) 1–7. doi:10.1002/fuce.20110005.
[35] American Society for Testing Material Committee, ASTM D828-97 (2002) Standard Test Method for Tensile Properties of Paper and Paperboard Using Constant Rate of Elongation Apparatus (Withdrawn 2009), ASTM International, West Conshohocken, PA, 2002.
[36] QuinTech - Brennstoffzellen Technologie. [Online] Available: http://www.quintech.de/englisch/products/research/GasDistributionLayer.php. [Accessed: 16/11/11].
[37] Freudenberg FCCT - Fuel Cell Component Technologies, 2010. [Online] Available: http://www.freudenbergfcct.com/gdl.htm [Accessed: 02/02/12].
[38] German Institute for Standardization, DIN EN 29073-3, Textiles; Test Method for Nonwovens; Part 3: Determination of Tensile Strength and Elongation (ISO 9073-3:1989), American National Standards Institute, 1992.
[39] T.F. Hung, J. Huang, H.J. Chuang, S.H. Bai, Y.J. Lai, Y.W. Chen-Yang, J. Power Sources 184 (2008) 165–171.
[40] American Society for Testing Material Committee, ASTM D638-10 Standard Test Method for Tensile Properties of Plastics, ASTM International, West Conshohocken, PA, 2010.
[41] T. Ha, J. Cho, J. Park, K. Min, H. Kim, E. Lee, J. Jyoung, Int. J. Hydrogen Energy 36 (2011) 12436–12443.
[42] I. Nitta, Inhomogeneous Compression of PEMFC Gas Diffusion Layers, PhD Dissertation, Department of Engineering Physics, Helsinki University of Technology, 2008.
[43] K. Han, B.K. Hong, S.H. Kim, B.K. Ahn, T.W. Lim, Int. J. Hydrogen Energy 36 (2011) 12452–12464.
[44] Y.-H. Lai, Y. Li, J.A. Rock, J. Power Sources 195 (2010) 3215–3223.
[45] E. Sadeghi, N. Djilali, M. Bahrami, J. Power Sources 195 (2010) 8104–8109.
[46] ASTM F36-99, Standard Test Method for Compressibility and Recovery of Gasket Materials, ASTM International, West Conshohocken, PA, 2009.
[47] International Organization for Standardization, ISO 5636-5:2003, 2011. [Online] Available: http://www.iso.org/iso/iso_catalogue/catalogue_tc/catalogue_detail.htm?csnumber=37376. [Accessed: 14/09/11].
[48] University of Cambridge: Symmetrical 3-point bending. [Online] Available: http://www.doitpoms.ac.uk/tlplib/beam_bending/3_point_bending.php. [Accessed: 20/02/12].
[49] D790-10, Standard Test Methods for Flexural Properties of Unreinforced and Reinforced Plastics and Electrical Insulating Materials, ASTM International, West Conshohocken, PA, 2010.
[50] R. Mathur, P. Maheswari, T. Dhami, R. Tandon, Electrochim. Acta 52 (2007) 4809–4817.
[51] R.B. Mathur, P.H. Maheshwari, T.L. Dhami, R.K. Sharma, C.P. Sharma, J. Power Sources 161 (2006) 790–798.
[52] D1184-98, Standard Test Method for Flexural Strength of Adhesive Bonded Laminated Assemblies, ASTM International, West Conshohocken, PA, 2004.
[53] C.S. Kong, D.Y. Kim, H.K. Lee, Y.G. Shul, T.H. Lee, J. Power Sources 108 (2002) 185–191.
[54] H.S. Chu, C. Yeh, F. Chen, J. Power Sources 123 (2003) 1–9.
[55] P. Cheung, J.F. Fairweather, D.T. Schwartz, Rev. Sci. Instrum. 82 (2011) 095102.
[56] R.B. Mathur, P.H. Maheshwari, T.L. Dhami, R.P. Tandon, Electrochim. Acta 52 (2007) 4809–4817.
[57] ASTM C188-09, Standard Test Method for Density of Hydraulic Cement, ASTM International, West Conshohocken, PA, 2009.
[58] C. Lim, C.Y. Wang, Electrochim. Acta 49 (2004) 4149–4156.
[59] I.R. Harkness, N. Hussain, L. Smith, J.D.B. Sharman, J. Power Sources 193 (2009) 122–129.
[60] A. Jena, K. Gupta, Chem. Eng. Technol. 33 (2010) 1241–1250.
[61] A. Jena, K. Gupta, Characterization of pore structure of fuel cell components containing hydrophobic and hydrophilic pores, in: 41st Power Sources Conference, June 14–17, Adams Mark Hotel, Philadelphia, Pennsylvania, 2004 [Online] Available, http://www.pmiapp.com/publications/index.html Accessed: 08/03/12].
[62] American Society for Testing Material Committee, ASTM F316-F303 (2011). Standard test methods for pore size characteristics of membrane filters by bubble point and mean flow pore test.
[63] A.M. Kannan, L. Munukutla, J. Power Sources 167 (2007) 330–335.
[64] M.A. Abdelkareem, T. Yoshitoshi, T. Tsujiguchi, N. Nakagawa, J. Power Sources 195 (2010) 1821–1828.
[65] P.M. Wilde, M. Maendle, M. Murata, N. Berg, Fuel Cells 4 (2004) 180–184.
[66] J.P. Feser, A.K. Prasad, S.G. Advani, J. Power Sources 162 (2006) 1226–1231.
[67] Gurley Precision Instruments, Air permeability, softness & smoothness [Online] Available: http://www.gurley.com/test/air.htm. [Accessed: 16/03/12].
[68] X. Wang, T.V. Nguyen, D.S. Hussey, D.L. Jacobson, J. Electrochem Soc. 157 (2010) B1777–B1782.
[69] G. Selvarani, A.K. Sahu, P. Sridhar, S. Pitchumani, A.K. Shukla, J. Appl. Electrochem. 38 (2007) 357–362.
[70] X. Wang, H. Zhang, J. Zhang, H. Xu, Z. Tian, J. Chen, H. Zhong, Y. Liang, B. Yi, Electrochim. Acta 51 (2006) 4909–4915.
[71] J.T. Gostick, M.W. Fowler, M.D. Pritzker, M.A. Ioannidis, L.M. Behra, J. Power Sources 162 (2006) 228–238.
[72] I.S. Hussaini, C.Y. Wang, J. Power Sources 195 (2010) 3830–3840.
[73] F.E. Hizir, S.O. Ural, E.C. Kumbur, M.M. Mench, J. Power Sources 195 (2010) 3463–3471.
[74] A.M. Kannan, P. Kanagala, V. Veedu, J. Power Sources 192 (2009) 297–303.
[75] L. Cindrella, A.M. Kannan, Fuel Cells 10 (2010) 563–566.
[76] R.J. Good, L.A. Girifalco, J. Phys. Chem. 64 (1960) 561–565.
[77] V. Gurau, M.J. Bluemle, E.S. De Castro, Y.-M. Tsou, J.A. Mann, T.A. Zawodzinski, J. Power Sources 160 (2006) 1156–1162.
[78] J.T. Gostick, M.W. Fowler, M.A. Ioannidis, M.D. Pritzker, Y.M. Volfkovich, A. Sakars, J. Power Sources 156 (2006) 375–387.
[79] E.W. Washburn, Phys. Rev. 17 (1921) 273–283.
[80] D. Owens, R. Wendt, J. Appl. Polym. Sci. 13 (1969) 1741–1747.
[81] E. Wang, P. Shi, C. Du, Electrochem. Comm. 10 (2008) 555–558.
[82] Y. Pai, J. Ke, H. Huang, C. Lee, J. Zen, F. Shieu, J. Power Sources 161 (2006) 275–281.
[83] A. Lee, W. Mérida, J. Power Sources 164 (2007) 141–153.
[84] S. Park, B.N. Popov, Fuel 88 (2009) 2068–2073.
[85] K. Jiao, X. Li, Int. J. Hydrogen Energy 35 (2010) 9095–9103.
[86] A. Theodorakakos, T. Ous, M. Gavaises, J.M. Nouri, N. Nikolopoulos, H. Yanagihara, J. Colloid Interface Sci. 300 (2006) 673–687.
[87] J. Benziger, J. Nehlsen, D. Blackwell, T. Brennan, J. Itescu, J. Membr. Sci. 261 (2005) 98–106.
[88] J. Speder, Effect of Potential Cycling on Platinum Electrocatalysts in the Presence of Chloride Anions, Ph.D. Dissertation, Department of Physics and Chemistry, University of Southern Denmark, 2010.
[89] Y. Shao, G. Yin, J. Zhang, Y. Gao, Electrochim. Acta 51 (2006) 5853–5857.
[90] K.H. Kangasniemi, D.A. Condit, T.D. Jarvi, J. Electrochem. Soc. 151 (2004) E125–E132.
[91] P.K. Sinha, P.P. Mukherjee, C.Y. Wang, J. Mat. Chem. 17 (2007) 3089–3103.
[92] P.K. Sinha, C.Y. Wang, Electrochim. Acta 52 (2007) 7936–7945.
[93] J.H. Nam, M. Kaviany, Int. J. Heat Mass Transfer 46 (2003) 4595–4611.
[94] V.P. Schulz, J. Becker, A. Wiegmann, P.P. Mukherjee, C.Y. Wang, J. Electrochem. Soc. 154 (2007) B419–B426.

[95] J.T. Gostick, M.A. Ioannidis, M.W. Fowler, M.D. Pritzker, J. Power Sources 173 (2007) 277–290.
[96] R. Wu, X. Zhu, Q. Liao, H. Wang, Y.-D. Ding, J. Li, D.-D. Ye, Int. J. Hydrogen Energy 35 (2010) 7588–7593.
[97] J. Hinebaugh, A. Bazylak, J. Electrochem. Soc. 157 (2010) B1382–B1390.
[98] B. Markicevic, N. Djilali, J. Power Sources 196 (2011) 2725–2734.
[99] S.P. Kuttanikkad, M. Prat, J. Pauchet, J. Power Sources 196 (2011) 1145–1155.
[100] G. Luo, Y. Ji, C.Y. Wang, P.K. Sinha, Electrochim. Acta 55 (2010) 5332–5341.
[101] O. Chapuis, M. Prat, M. Quintard, E. Chane-Kane, O. Guillot, N. Mayer, J. Power Sources 178 (2008) 258–268.
[102] S. Succi, E. Foti, F. Higuera, Europhysics Lett. 10 (1989) 433.
[103] D.H. Rothman, J.M. Keller, J. Stat. Phys. 52 (1988) 1119–1127.
[104] A. Pan, M. Hilpert, C.T. Miller, Water Resour. Res. 40 (2004) W01501.
[105] P.P. Mukherjee, C.Y. Wang, Q.J. Kang, Electrochim. Acta 54 (2009) 6861–6875.
[106] L. Hao, P. Cheng, J. Power Sources 186 (2009) 104–114.
[107] L. Hao, P. Cheng, J. Power Sources 195 (2010) 3870–3881.
[108] X. Shan, H. Chen, Phy. Rev. E 47 (1993) 1815–1819.
[109] M.R. Swift, E. Orlandini, W.R. Osborn, J.M. Yeomans, Phys. Rev. E 54 (1996) 5041–5052.
[110] L. Chen, H.B. Luan, Y.L. He, W.Q. Tao, Int. J. Thermal Sci. 51 (2012) 132–144.
[111] M.V. Williams, H.R. Kunz, J.M. Fenton, J. Electrochem. Soc. 151 (2004) A1617–A1627.
[112] G. Chen, H. Zhang, H. Ma, H. Zhong, Int. J. Hydrogen Energy 34 (2009) 8185–8192.
[113] Y. Lee, B. Kim, Y. Kim, X. Li, Appl. Energy 88 (2011) 5111–5119.
[114] T. Ha, J. Cho, J. Park, K. Min, H.-S. Kim, E. Lee, J.-Y. Jyoung, Int. J. Hydrogen Energy 36 (2011) 12427–12435.
[115] J.F. Kumar, V. Radhakrishnan, P. Haridoss, Int. J. Hydrogen Energy 36 (2011) 7207–7211.
[116] A. Lasia, in: B.E. Conway, J. Bockris, R.E. White (Eds.), Modern Aspects of Electrochemistry, Kluwer Academic/Plenum Publishers, New York, 1999, pp. p.143–248.
[117] S.R. Taylor, E. Gileadi, Corr. Sci. 51 (1995) 664–667.
[118] R. de Leviein, P. Delahay (Eds.), Advances in Electrochemistry and Electrochemical Engineering, Interscience, New York, 1967, p. p.329.
[119] J. Lobato, P. Cañizares, M.A. Rodrigo, J.J. Linares, in: Monwar Hossain (Ed.), Heat and Mass Transfer – Modeling and Simulation, InTech, September 2011, ISBN 978-953-307-604-1, pp. 17–40.
[120] G. Dotelli, L. Omati, P.G. Stampino, P. Grassini, D. Brivio, J. Power Sources 196 (2011) 8955–8966.
[121] P.G. Stampino, L. Omati, G. Dotelli, J. Fuel Cell Sci. Tech. 8 (2011) 41005.
[122] Z. Tang, C.K. Poh, Z.Q. Tian, J.Y. Lin, H.Y. Ng, D.H.C. Chua, Electrochim. Acta 56 (2011) 4327–4334.
[123] H.M. Chang, C.W. Lin, M.H. Chang, H.R. Shiu, W.C. Chang, F.H. Tsau, J. Power Sources 196 (2011) 3773–3780.
[124] K. Nakagawa, Y. Yasumura, N. Thongprachan, N. Sano, Chem. Eng. Process. 50 (2011) 22–30.
[125] Y. Gao, G.Q. Sun, S.L. Wang, S. Zhu, Energy 3 (2010) 1455–1459.
[126] G.B. Chen, H.M. Zhang, H.P. Ma, H.X. Zhong, Int. J. Hydrogen Energy 34 (2009) 8185–8192.
[127] C.Y. Du, B.R. Wang, X.Q. Cheng, J. Power Sources 187 (2009) 505–508.
[128] Y. Gao, G.Q. Sun, S.L. Wang, H. Sun, Q. Mao, Energy Fuels 22 (2008) 4098–4101.
[129] A. Kramer, S.A. Freunberger, R. Flueckiger, I.A. Schneider, A. Wokaun, F.N. Buechi, G.G. Scherer, J. Electroanal. Chem. 612 (2008) 63–77.
[130] D. Cheng, S.Y. Ye, E. Gyenge, Electrochem. Solid State Lett. 11 (2008) 148–152.
[131] M. Rosli, D. Borman, D. Ingham, J. Fuel Cell Sci. Tech. 7 (2010) 061015.
[132] J. Wu, X. Ziyuan, H. Wang, M. Blanco, J. Martin, J. Zhang, Int. J. Hydrogen Energy 33 (2008) 1747–1757.
[133] A. Bazylak, Int. J. Hydrogen Energy 34 (2009) 3845–3857.
[134] K. Jiao, J. Park, X. Li, Appl. Energy 87 (2010) 2770–2777.
[135] D. Spernjak, A.K. Prasad, S.G. Advani, J. Power Sources 170 (2007) 334–344.
[136] K.S.S. Naing, Y. Tabe, T. Chikahisa, J. Power Sources 196 (2011) 2584–2594.
[137] M.M. Daino, Z. Lu, J.M. La Manna, J.P. Owejan, T.A. Trabold, S.G. Kandlikar, Electrochem. Solid State Lett. 14 (2011) B51–B54.
[138] K. Nishida, M. Ishii, S. Tsushima, S. Hirai, J. Power Sources 199 (2012) 155–160.
[139] M. Matian, A.J. Marquis, N.P. Brandon, Int. J. Hydrogen Energy 35 (2010) 12308–12316.
[140] R.J. Bellows, M.Y. Lin, M. Arif, A.K. Thompson, D. Jacobson, J. Electrochem. Soc. 146 (1999) 1099–1103.
[141] C. Hartnig, I. Manke, in: J. Garche (Ed.), Encyclopedia of Electrochemical Power Sources, Elsevier, Amsterdam, 2009, pp. 738–757.
[142] P. Quan, M.C. Lai, D.S. Hussey, D.L. Jacobson, A. Kumar, S. Hirano, J. Fuel Cell Sci. Tech. 7 (2010) 051009–051016.
[143] D.S. Hussey, D.L. Jacobson, M. Arif, K.J. Coakley, D.F. Vecchia, J. Fuel Cell Sci. Tech. 7 (2010) 021024.
[144] R. Satija, D.L. Jacobson, M. Arif, S.A. Werner, J. Power Sources 129 (2004) 238–245.
[145] A. Turhan, K. Heller, J.S. Brenizer, M.M. Mench, J. Power Sources 180 (2008) 773–783.
[146] D. Kramer, J. Zhang, R. Shimoi, E. Lehmann, A. Wokaun, K. Shinohara, G. Scherer, Electrochim. Acta 50 (2005) 2603–2614.
[147] P. Oberholzer, P. Boillat, R. Siegrist, R. Perego, A. Kästner, E. Lehmann, G.G. Scherer, A. Wokaun, J. Electrochem. Soc. 159 (2012) B235.
[148] I. Manke, C. Hartnig, M. Grünerbel, J. Kaczerowski, W. Lehnert, N. Kardjilov, A. Hilger, J. Banhart, W. Treimer, M. Strobl, Appl. Phys. Lett. 90 (2007) 184101.
[149] C. Tötzke, I. Manke, T. Arlt, H. Markötter, N. Kardjilov, A. Hilger, S.H. Williams, P. Krüger, R. Kuhn, C. Hartnig, J. Scholta, J. Banhart, Nucl. Instrum. Methods Phys. Res. Sect. A 663 (2012) 48–54.
[150] T. Kim, C. Sim, M. Kim, Appl. Radiat. Isot. 66 (2008) 593–605.
[151] I. Manke, C. Hartnig, N. Kardjilov, H. Riesemeier, J. Goebbels, R. Kuhn, P. Krüger, J. Banhart, Fuel Cells 10 (2009) 26–34.
[152] J. Owejan, T. Trabold, D. Jacobson, M. Arif, S. Kandlikar, Int. J. Hydrogen Energy 32 (2007) 4489–4502.
[153] J. Owejan, T. Trabold, J. Gagliardo, D. Jacobson, R. Carter, D. Hussey, M. Arif, J. Power Sources 171 (2007) 626–633.
[154] Y.-S. Chen, H. Peng, J. Fuel Cell Sci. Tech. 6 (2009) 031016–031113.
[155] T. Kim, J. Kim, C. Sim, S. Lee, M. Kaviany, S. Son, M. Kim, Nucl. Instrum. Methods Phys. Res. Sect. A 600 (2009) 325–327.
[156] J. Park, X. Li, D. Tran, T. Abdelbaset, D. Hussey, D. Jacobson, M. Arif, Int. J. Hydrogen Energy 33 (2008) 3373–3384.
[157] C. Hartnig, I. Manke, N. Kardjilov, A. Hilger, M. Grunerbel, J. Kaczerowski, J. Banhart, W. Lehnert, J. Power Sources 176 (2008) 452–459.
[158] P. Boillat, D. Kramer, B.C. Seyfang, G. Frei, E. Lehmann, G. Scherer, A. Wokaun, Y. Ichikawa, Y. Tasaki, K. Shinohara, Electrochem. Commun. 10 (2008) 546–550.
[159] A. Lange, A. Kupsch, M.P. Hentschel, I. Manke, N. Kardjilov, T. Arlt, R. Grothausmann, J. Power Sources 196 (2011) 5293–5298.
[160] N. Takenaka, H. Asano, K. Sugimoto, H. Murakawa, N. Hashimoto, N. Shindo, K. Mochiki, R. Yasuda, Instrum. Methods Phys. Res. Sect. A 651 (2011) 277–281.
[161] S. Tsushima, S. Hirai, Prog. Energy Combust. Sci. 37 (2011) 204–220.
[162] I. Manke, C. Hartnig, M. Gruünerbel, W. Lehnert, N. Kardjilov, A. Haibel, A. Hilger, J. Banhart, H. Riesemeier, Appl. Phys. Lett. 90 (2007) 174105.
[163] T.T. Mukaide, S. Mogi, J. Yamamoto, A. Morita, S. Koji, K. Takada, K. Uesugi, K. Kajiwara, T. Noma, J. Synchrotron Radiat. 15 (2008) 329–334.
[164] C. Hartnig, I. Manke, R. Kuhn, N. Kardjilov, J. Banhart, W. Lehnert, Appl. Phys. Lett. 92 (2008) 134106.
[165] P. Krüger, H. Markötter, J. Haußmann, M. Klages, T. Arlt, J. Banhart, C. Hartnig, I. Manke, J. Scholta, J. Power Sources 196 (2011) 5250–5255.
[166] S.J. Lee, N.-Y. Lim, S. Kim, G.-G. Park, C.-S. Kim, J. Power Sources 185 (2008) 867–870.
[167] S. Tsushima, S. Hirai, Fuel Cells 9 (2009) 506–517.
[168] A. Iranzo, M. Munoz, F. Rosa, J. Pino, Int. J. Hydrogen Energy 35 (2010) 11533–11550.
[169] J. Becker, C. Wieser, S. Fell, K. Steiner, Int. J. Heat Mass Transfer 54 (2011) 1360–1368.
[170] I. Taymaz, M. Benli, Energy 35 (2010) 2134–2140.
[171] Y.-H. Lai, P.A. Rapaport, C. Ji, V. Kumar, J. Power Sources 184 (2008) 120–128.
[172] T. Hottinen, O. Himanen, S. Karvonen, N. Iwao, J. Power Sources 171 (2007) 113–121.
[173] Z. Shi, X. Wang, J. Power Sources 185 (2008) 985–992.
[174] V. Radhakrishnam, P. Haridoss, Mater. Des. 32 (2011) 861–868.
[175] P.A. Garcia-Salaberri, M. Vera, R. Zaera, Int. J. Hydrogen Energy 36 (2011) 11856–11870.
[176] R. Mukundan, Y.S. Kim, T. Rockward, J.R. Davey, B. Pivovar, D.S. Hussey, D.L. Jacobson, M. Arif, R. Borup, ECS Trans. 11 (2007) 543–552.
[177] S.-J. Lim, G.-G. Park, J.-S. Park, Y.-J. Sohn, S.-D. Yim, T.-H. Yang, B.K. Hong, C.-S. Hong, C.-S. Kim, Int. J. Hydrogen Energy 35 (2010) 13111–13117.